processes

MDPI

Article

In Vitro Degradation of Continuous Iron Wire-Reinforced PLLA Composite Monofilaments for Bioresorbable Vascular Stents Fabricated via a Novel 3D Printer: An Early-Stage Prototype Study

Handai Liu [1], Alexandre Portela [2], Han Xu [1], Vlasta Chyzna [1], Yinshi Lu [1], Ke Gong [1], Daniel P. Fitzpatrick [3], Guangming Yan [4], Ronan Dunbar [5] and Yuanyuan Chen [1,*]

[1] Polymer, Recycling, Industrial, Sustainability and Manufacturing (PRISM) Research Institute, Athlone Campus, Technological University of the Shannon: Midlands Midwest, N37 HD68 Athlone, Ireland; a00237386@student.tus.ie (H.L.); a00258805@student.tus.ie (H.X.); a00290622@student.tus.ie (Y.L.); ke.gong@tus.ie (K.G.)
[2] Department of Environment & Climate Action, Tipperary County Council, E91 N512 Clonmel, Ireland
[3] Centre of Industrial Services and Design, Technological University of the Shannon: Midlands Midwest, N37 HD68 Athlone, Ireland
[4] Applied Polymer Technologies Gateway Centre, Technological University of the Shannon: Midlands Midwest, N37 HD68 Athlone, Ireland
[5] Engineering & Informatics Department, Technological University of the Shannon: Midlands Midwest, N37 HD68 Athlone, Ireland
* Correspondence: yuanyuan.chen@tus.ie

Abstract

Poly(L-lactic acid) (PLLA) and iron (Fe) are popular bioresorbable material candidates for biomedical implants. However, PLLA coronary stents are relatively too thick compared to metallic stents when providing the same mechanical strength, while iron degrades too slowly. Recent studies show that PLLA coatings can enhance iron's corrosion rate, and iron has strong mechanical strength, making PLLA–Fe composites ideal for bioresorbable implants. Although PLLA coatings on iron samples have been studied, research on embedding iron wires in relatively thick PLLA matrices is limited. Moreover, no studies have yet explored 3D-printed metal wire-reinforced PLLA monofilaments for biomedical applications. To address these research gaps and investigate the in vitro degradation profile of PLLA/Fe wire monofilaments for bioresorbable stents, this study first developed a novel polymer filament–metal wire coextrusion 3D printer for printing PLLA/Fe wire monofilaments. In vitro degradation tests were then conducted on both PLLA/Fe and neat PLLA monofilaments at 50 °C. Thereafter, characterizations, including mass loss, pH, surface appearance and morphology, tensile tests, gel permeation chromatography (GPC), and differential scanning calorimetry (DSC), were performed. Results indicated that the overall degradation rate of PLLA/Fe monofilaments was higher than that of PLLA counterparts, while the degradation rate of PLLA matrix was not affected by the embedded iron wire according to molecular weight analysis. Notably, the Young's modulus and stiffness of PLLA monofilaments were significantly improved by the iron wires during the early stages of degradation, but the reinforcement in tensile strength was negative after immersion due to the poor embedding quality of the iron wires in the PLLA monofilaments. With future improvement of the embedding quality of iron wire, the 3D-printed PLLA/Fe wire composites can have great potential in the development of biomedical devices using the novel 3D printing method, including most types of stents and bone scaffolds.

check for updates

Academic Editor: Tao Sun

Received: 21 June 2025
Revised: 13 August 2025
Accepted: 15 August 2025
Published: 19 August 2025

Citation: Liu, H.; Portela, A.; Xu, H.; Chyzna, V.; Lu, Y.; Gong, K.; Fitzpatrick, D.P.; Yan, G.; Dunbar, R.; Chen, Y. In Vitro Degradation of Continuous Iron Wire-Reinforced PLLA Composite Monofilaments for Bioresorbable Vascular Stents Fabricated via a Novel 3D Printer: An Early-Stage Prototype Study. *Processes* **2025**, *13*, 2621. https://doi.org/10.3390/pr13082621

Copyright: © 2025 by the authors. Licensee MDPI, Basel, Switzerland. This article is an open access article distributed under the terms and conditions of the Creative Commons Attribution (CC BY) license (https://creativecommons.org/licenses/by/4.0/).

Keywords: 3D printing; polymer–metal wire composite; PLLA; iron wire; in vitro degradation; coextrusion

1. Introduction

Presently, coronary artery disease (CAD) is one of the leading causes of morbidity and mortality in modern society worldwide [1–3]. The use of stents in percutaneous coronary intervention (PCI), as the gold standard treatment for CADs [4], has progressively developed over the past 35 years [5,6]. Currently, the employment of the latest drug-eluting stent (DES) can still result in persistent inflammatory responses and late stent thrombosis (ST) due to delayed vascular reendothelialization and the permanent presence of the metal implant [2,7,8]. With the expectation of addressing the complications caused by permanent implants in vessels, researchers worldwide have focused intensively on the development of the bioresorbable vascular stent (BVS) [9]. The BVS is made of bioresorbable materials and is designed to provide short-term mechanical support to reopen the narrowed artery, gradually resorb, and be excreted by the body after vascular remodeling and recovery [9].

Generally, BVSs can be categorized into two main types based on their building materials: biodegradable polymers, such as polylactic acid (PLA), polyglycolic acid (PGA), polycaprolactone (PCL), and poly(lactic-co-glycolic acid) (PLGA), and biodegradable metals, including magnesium (Mg), iron (Fe), zinc (Zn), and their respective alloys [9–11]. The first U.S. Food and Drug Administration (FDA)-approved BVS was the Absorb Bioresorbable Vascular Scaffold (Absorb™ BVS), released in 2016 [12]. However, it was withdrawn from the market in 2017 due to an increased rate of late-stage ST and target lesion failure [13–15]. The thick structure (157 μm) of the Absorb™ BVS is widely regarded as the primary reason for these issues [16–18]. This implies that the mechanical strength of the PLLA matrix needs to be improved to build thinner (around 50–100 μm) BVSs [12,19–21]. Additionally, some studies have pointed out that the reduced pH in local areas surrounding the stent can induce inflammatory reactions caused by acidic degradation by-products, which is another critical concern [15,22–24].

On the other hand, iron-based BVSs have gained increasing interest from researchers due to their excellent mechanical performance, biocompatibility, and advancements in iron alloy techniques and surface treatments [14,25,26]. To develop potential iron-based BVSs, two main concerns must be addressed effectively: the low degradation rate and the by-products of iron corrosion [27]. Recently, some studies have demonstrated that incorporating alkaline metals or metal oxides, such as Mg, Zn, Fe, MgO, and ZnO, into aliphatic polyesters, such as PLA, PGA, PLGA, and Poly(D, L-lactic acid) (PDLLA), can neutralize acidic degradation by-products and accelerate the degradation process [28–35]. In the field of iron-based PLA coating composites, Zhang et al. elucidated the mechanism of accelerated degradation in iron–PLA biomaterials [4], while other researchers have demonstrated the long-term efficacy and safety of bioresorbable iron–PLA composite stents through continuous in vitro studies [16,36], in vivo studies [14,37], and a clinical application in human below-the-knee arteries [38]. Meanwhile, Gao et al. [39] demonstrated the accelerated degradation of nitriding treatment and PDLLA coating on iron-based composite stents. They also reported a 3-year follow-up of the first-in-human evaluation of the ultrathin iron bioresorbable scaffold (IBS), with positive and promising outcomes in 2024. However, the complete absorption periods of these promising iron-based aliphatic polyester composite stents remain longer than the ideal period of 1–2 years [40,41], which could be attributed to the low percentage of the aliphatic polyester layer. Therefore, it would be highly interesting to investigate the mechanical and degradation performance

of iron–aliphatic polyester composite stents when polymers serve as the dominant matrix. Moreover, the authors speculate that a lower percentage of iron could reduce the formation of insoluble iron corrosion by-products, which require a long time for surrounding tissues to absorb and excrete [26,27]. To make the most of the merits of both PLLA and iron materials, it is hypothesized that incorporating iron wire into the PLLA matrix can not only enhance the mechanical performance but also increase the degradation rate of PLLA/Fe composites.

With the development of 3D printing technology, a significantly growing number of researchers have adopted 3D printers in the field of medical device development over the past decades [11,42,43]. In the area of material extrusion 3D printing of polymer-based stents, researchers have demonstrated the feasibility of printing vascular stents using pristine polymers [44–47], polymer blends [48,49], metallic or bioinorganic nanosheet or particle-reinforced polymer composites [50–53], and short fiber-reinforced polymer composites [54,55]. However, to the best of our knowledge, no studies have been published to date in the specific field of metal wire–polymer coextrusion 3D printing for the fabrication and evaluation of medical implants. While several papers have demonstrated the coextrusion 3D printing of continuous metal wire-reinforced polymer composites, their focus has been limited to simple mechanical test specimens [56–59], block samples for thermal conductivity studies [60,61], or sensing applications [62–64], primarily using copper or steel wire. Therefore, it is essential to demonstrate the feasibility of 3D printing continuous iron wire-reinforced polymer thin monofilaments. This would enable the fabrication of metal wire-reinforced polymer stents by integrating the novel coextrusion process with recently developed four-axis material extrusion-based 3D printers [48,49]. Furthermore, the preliminary evaluation of these 3D-printed monofilaments can provide valuable insights for the practical and systematic development of metal wire-reinforced polymer stents.

Based on the aforementioned knowledge, this study employed PLLA and iron wire to develop a PLLA/Fe wire composite for BVSs, with the hypothesis that incorporating iron wire into PLLA monofilaments would not only enhance the mechanical properties of PLLA but also accelerate the degradation rate of the composite. Therefore, this study first developed a novel polymer filament–metal wire coextrusion 3D printer. Thereafter, PLLA/Fe wire monofilaments were fabricated, while pure PLLA monofilaments printed under the same parameters served as the control group. Finally, the in vitro degradation performance of the PLLA/Fe wire composite monofilaments was evaluated to establish a foundation for future research on PLLA/Fe wire BVSs.

2. Materials and Methods

2.1. Materials

PLLA filament was obtained from 3D4MAKERS (Haarlem, The Netherlands). More specific properties of this filament are listed in Table 1 according to its Technical Data Sheet (TDS). Before being fed into the FME printer, the filament was dried at 40 °C overnight and stored in a vacuum-sealed package. Pure iron spooled wire (purity: 99.5%, length: 2000 m) was purchased from Goodfellow Cambridge Ltd. (Cambridgeshire, UK). The main information of the iron wire is provided in Table 1 as well. The reagents for simulated body fluid (SBF) preparation are listed in Table 2 including NaCl, $NaHCO_3$, KCl, $K_2HPO_4 \cdot 3H_2O$, $MgCl_2 \cdot 6H_2O$, 1M HCl, $CaCl_2$, Na_2SO_4, and Tris($(CH_2OH)_3CNH_2$). All materials were used as received.

2.2. A Novel Filament–Metal Wire Coextrusion 3D Printer

A novel filament–metal wire coextrusion 3D printer was developed by modifying a desktop open-source 2-in-1-out single-nozzle 3D printer (Geeetech A10M, Shenzhen Getech Technology Co., Ltd., Shenzhen, China) (Figure 1b). The modification involved

integrating a thin metal wire conduit positioned within the upper section of the nozzle's interior, with its central axis aligned to the nozzle's axis as shown in Figure 1a. This design facilitated the synchronized extrusion of the thin metal wire with the polymer filament, enabling in-nozzle impregnation during the extrusion process. The specific size of the dispensing stainless needle adopted was G22 (Shenzhen Hongyun Dispensing Accessories Co., Ltd., Shenzhen, China), with an outer diameter (OD) of 0.7 mm, an inner diameter (ID) of 0.4 mm, and a total length of 62 mm. A schematic diagram illustrating the working principle of the novel 3D printer is shown in Figure 1.

Table 1. Properties of PLLA filaments (3D4Makers) and iron wire (Goodfellow).

Property	PLLA	Iron Wire	Unit
Diameter	1.75	0.065	mm
Density	1.24	7.87	g/cm^3
Melt temperature	175	1535	°C
Nozzle temperature (recommended)	180–220	-	°C
Tensile strength at break	50	180–210	MPa
Tensile elongation at break	≤5%	-	
Young's modulus	3.5	211.4	GPa
Flexural modulus	3.35	-	GPa
Charpy impact strength	21	-	kJ/m^2

Table 2. Regents for preparing 1000 mL SBF (PH 7.4).

Order	Reagent	Amount	Supplier
1	NaCl (≥99.5%)	7.996 g	Sigma-Aldrich (Taufkirchen, Germany)
2	$NaHCO_3$ (≥99.5%)	0.350 g	Sigma-Aldrich (Taufkirchen, Germany)
3	KCl (≥99.0%)	0.224 gt	Honeywell (Seelze, Germany)
4	$K_2HPO_4 \cdot 3H_2O$ (≥99.0%)	0.228 g	Sigma-Aldrich (Taufkirchen, Germany)
5	$MgCl_2 \cdot 6H_2O$ (≥99.0%)	0.305 g	Sigma-Aldrich (Taufkirchen, Germany)
6	1.0 M-HCl	39 mL	TCI (Zwijndrecht, Belgium)
7	$CaCl_2$	0.278 g	Sigma-Aldrich (Taufkirchen, Germany)
8	Na_2SO_4 (≥99.0%)	0.071 g	Sigma-Aldrich (Taufkirchen, Germany)
9	$(CH_2OH)_3CNH_2$ (>99.0%)	6.057 g	TCI (Zwijndrecht, Belgium)
10	1.0 M-HCl: adjusting pH to 7.4	0–5 mL	TCI (Zwijndrecht, Belgium)

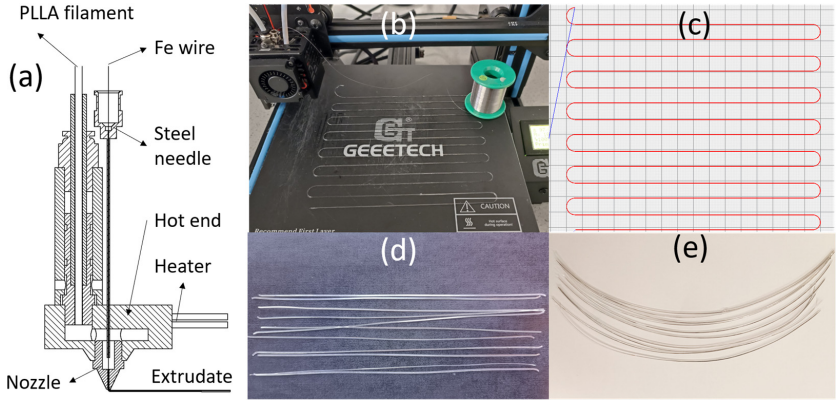


Figure 1. Schematic diagram of the filament–metal wire coextrusion head (**a**), demonstration of PLLA/Fe wire filament printing (**b**), S-path for monofilament printing (**c**), printed PLLA monofilaments (**d**), printed PLLA/Fe wire monofilaments (**e**).

2.3. Specimen Preparation

In this study, a total of 150 monofilaments were obtained from 15 S-path specimens printed using the novel 3D printer for both pure PLLA and PLLA/Fe wire samples. The iron wire used for the 3D printing of PLLA/Fe wire monofilaments had a diameter of 0.065 mm. The dimensions of 3D-printed monofilaments were measured using ImageJ software (version 1.51j8) based on their microscope images. The results indicated that the cross-sectional dimensions of neat PLLA and PLLA/Fe wire monofilaments were $292.40 \pm 13.06 \times 617.38 \pm 23.53$ μm^2 and $310.30 \pm 36.77 \times 650.96 \pm 10.80$ μm^2, respectively, as shown in Table 3. All monofilaments were kept approximately 120 mm in length for tensile tests. Both PLLA/Fe wire and pure PLLA monofilaments were divided into 10 groups, with each group containing at least 10 samples for in vitro degradation and other tests. The G-code was generated by modifying the G-code of a similar geometry using the EasyPrint3D (v1.0.17) slicer. The same printing parameters (Table 4) and G-code were used for printing both pure PLLA and PLLA/Fe wire composite specimens. The direct printing path model of the S-path specimen is shown in Figure 1c, and the monofilaments are shown in Figure 1d,e. Samples for other tests, such as mass change, morphology imaging, GPC, DSC, and FTIR, were obtained from untested or tested specimens from tensile tests. In the final averaging of the test results, any outliers were excluded [65].

Table 3. The compositions of PLLA and PLLA/Fe wire monofilaments.

	PLLA/Fe Wire Monofilament		**Pure PLLA Monofilament**
Composition	PLLA	Iron wire	PLLA
Dimensions (μm)	$310.30 \pm 36.77 \times 650.96 \pm 10.80$	Ø 65.28 ± 0.41	$292.40 \pm 13.06 \times 617.38 \pm 23.53$

Table 4. The 3D printing parameters for the fabrication of PLLA and PLLA/Fe wire monofilaments.

Parameters	**Value**	**Unit**
Nozzle diameter	0.6	mm
Layer height	0.3	mm
Extrusion head temperature	200	°C
Bed temperature	60	°C
Cooling fan speed	100	%
Filling pattern	Line	
Fill angle (X axis)	±0	°
Filling density	100	%
Print speed on slicer	1.2	mm/s

2.4. In Vitro-Accelerated Degradation

2.4.1. Simulated Body Fluid (SBF) Preparation

To ensure the ion concentrations of the prepared SBF matched those in human blood plasma, the following substances (Table 4) were added to 850 mL of deionized water and stirred to prepare 1000 mL of SBF, following the method of Kokubo et al.: NaCl, $NaHCO_3$, KCl, $K_2HPO_4 \cdot 3H_2O$, $MgCl_2 \cdot 6H_2O$, 1M HCl, $CaCl_2$, Na_2SO_4, and Tris($(CH_2OH)_3CNH_2$), sequentially, according to Kokubo et al. [66]. During preparation, each reagent was fully dissolved before adding the next. The solution was titrated with 1 M HCl until the pH reached 7.25, with the temperature maintained at 36.5 °C using a water bath. Finally, the solution was transferred to a 1000 mL volumetric flask, and deionized water was added at 20 °C to adjust the solution to the required volume [67]. The prepared solution was transferred to a plastic bottle and stored in a refrigerator at 4–10 °C. The stored SBF solution was discarded if precipitation occurred.

2.4.2. Immersion Test

The in vitro-accelerated degradation tests were performed according to ISO 13781:2017 [68]. Before immersion in SBF, monofilaments were sterilized using 70% isopropyl alcohol for 3 min and rinsed three times with deionized water. The samples were then dried in a vacuum oven (Salvislab VC20, Rotkreuz, Switzerland) at 45 °C for 24 h before measuring the initial mass (M_0) of each monofilament. To prevent curling during accelerated degradation [69], each monofilament was secured to a polypropylene (PP) tube (diameter: 4 mm) by inserting it into three distributed holes, as shown in Figure 2a,b. Each group of monofilaments (n = 10) was vertically placed in a test tube (50 mL) with a stopper to prevent SBF evaporation [70]. It should be noted that both PLLA/Fe and PLLA samples for week 12, immersed in the last right tubes (Figure 2c,d), were not bound by a PP tube, and the samples were too curled to be separated and tested on a tensile tester. Fifty milliliters of prepared SBF (pH: 7.2–7.4) was transferred to each tube, ensuring the ratio of SBF solution to surface area and sample weight exceeded 50:1 mL/cm^2 and 30:1 mL/g, respectively, following ISO 13781 [71–74]. Specifically, the mean initial mass sums of PLLA/Fe and PLLA samples in each degradation tube were 356.60 ± 15.09 mg and 338.40 ± 4.95 mg, as shown in Table 5, with SBF solution-to-mass ratios of 140.20 and 147.75 mL/g, respectively. The sample tubes were placed in a circular orbit shaker incubator (New Brunswick Innova 4000, Hampton, VA, USA) at 50 °C for temperature-accelerated degradation, with an orbital shaking speed of 80 RPM to simulate the average adult heart rate [70]. The elevated temperature of 50 °C was chosen because it is below the glass transition temperature (T_g) of the samples, ensuring a reliable accelerated degradation mechanism [71,75,76]. Previous studies indicate that the in vitro degradation rate of PLLA at 50 °C is approximately four times faster than at the normal physiological temperature of 37 °C [71,74,77].

Table 5. The initial mass sum and mean of PLLA/Fe wire and PLLA monofilaments for each group.

Initial Mass Sum of the Monofilament Group in Each Degradation Tube (mg)										
Groups	**Week_1**	**Week_2**	**Week_3**	**Week_4**	**Week_5**	**Week_6**	**Week_8**	**Week_10**	**Week_12**	**Mean ± SD**
PLLA/Fe	327.88	378.86	363.7	349.13	364.74	343.11	355.79	357.59	368.62	356.60 ± 15.09
PLLA	333.18	341.44	339.33	340.86	345.52	336.56	336.98	342.36	329.39	338.40 ± 4.95

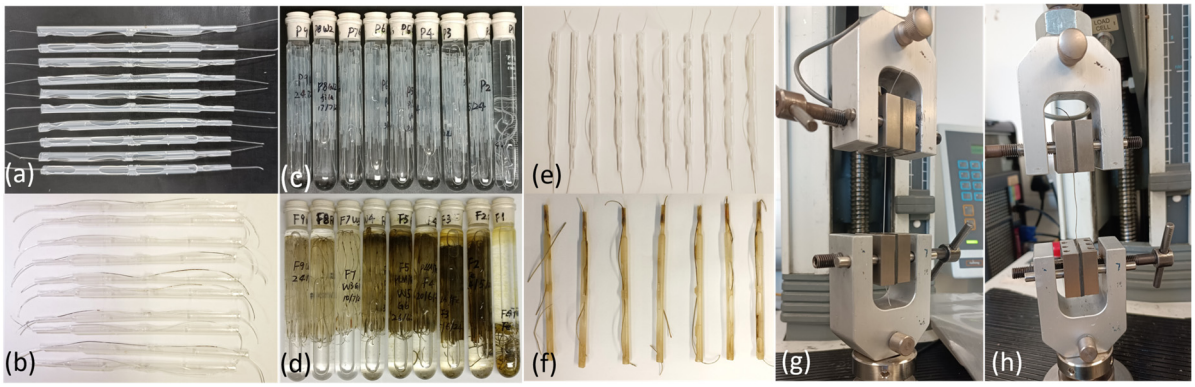


Figure 2. Monofilaments bound in PP tubes, immersed in testing tubes, degraded 6 weeks, and under testing were shown in figures (**a**,**c**,**e**,**g**) for PLLA, and figures (**b**,**d**,**f**,**h**) for PLLA/Fe composite samples, respectively.

The specimen tubes were placed in the shaker incubator for 1, 2, 3, 4, 5, 6, 8, 10, and 12 weeks. For clarity, each group of pure PLLA and continuous iron wire-reinforced PLLA composite monofilaments was denoted as PLLA_0, PLLA_1 to PLLA_12, and PLLA/Fe_0, PLLA/Fe_1 to PLLA/Fe_12 for immersion weeks 0 to 12, respectively. The SBF solution was replaced with fresh SBF weekly, and pH values were measured using a pH meter

(JENWAY 3520, Dunmow, UK) before replacement. All sample tubes were collected at the end of week 12.

2.4.3. Iron Ion Concentration Measurement

An iron test kit (0.01–0.2 mg/L, MQuant) purchased from Sigma-Aldrich was used to measure the iron released in the degradation solutions. All iron ions were reduced to iron (II) ions by adding the Fe reagents from the colorimetric kit; therefore, this test kit measured the total iron content in the degradation solution released from the samples. The measurements were conducted on the degradation solutions of the PLLA/Fe samples at the final collection time point (week 12). According to the testing guide, 100 µL of each degradation solution was first transferred to sample tube B before being diluted to 20 mL (200×). Thereafter, five drops of Fe reagents were added to sample tube B to initiate the reduction and colorimetric reactions, forming a red–violet complex. Meanwhile, control tube A was filled with 20 mL of distilled water. After a three-minute reaction, the iron concentration was determined by visually comparing the color of the measurement solution with the color fields on a standard color card. This kit allows precise analysis due to its fine color gradation. The initial results were multiplied by 200 following the dilution procedure.

2.5. Tensile Test

To account for the wet environment in the SBF solution, the collected samples were directly subjected to uniaxial tensile testing using a Lloyd LRX universal tester (Lloyd Instruments Ltd., Bognor Regis, UK) equipped with a 50 N load cell and rubber-faced grips. The tests were conducted at a fixed loading speed of 1 mm/min under laboratory environmental conditions (temperature: 20 ± 2 °C, relative humidity: 50 ± 5%) and a gauge length of 50 mm under ASTM D3822/D3822M-14 [78]. Test data were recorded using Nexygen™ (v 4.2) software [79]. At least three replicates from each group were tested, and the thickness and width of each specimen were measured using a digital vernier caliper prior to testing. Data, including stress at maximum load, percentage strain at maximum load, stiffness, and Young's modulus, were recorded and statistically analyzed using SPSS Statistics (IBM version 28).

2.6. Mass Loss Percentage

After tensile testing, the samples were ultrasonically cleaned in deionized water for 10 min, rinsed twice with deionized water, and dried sequentially using filter papers to absorb excess water. The samples were then dried in a vacuum oven at 45 °C for 24 h. The weight (M_1) of each monofilament after degradation was measured using a Sartorius scale (MC 210 P) with a resolution of 10^{-5} g [80], excluding defective samples. The mass loss percentage of each monofilament was calculated using Equation (1) [70,81]:

$$\text{Mass loss (\%)} = (M_0 - M_1)/M_0 \times 100\% \quad (1)$$

where M_0 is the initial mass of the monofilament before degradation, and M_1 is the dried mass of the monofilament after degradation.

2.7. Gel Permeation Chromatography (GPC) Test

The number-average molecular weight (M_n), weight-average molecular weight (M_w), peak molecular weight (M_p), and molar mass dispersity ($Đ_M = M_w/M_n$ [82]) of all PLLA and PLLA/Fe wire composite monofilament groups were determined using a gel permeation chromatography (GPC) system (1260 Infinity II, Agilent Technologies, Santa Clara, CA, USA) [83]. To prepare PLLA/Fe wire composite samples for GPC testing, approximately 150 mg of degraded PLLA/Fe wire sample from each group was completely dissolved

in 4 mL HFIP (1,1,1,3,3,3-hexafluoro-2-propanol) solvent. The solution was then transferred to glass Petri dishes using a syringe with a 13 mm PTFE filter (0.20 μm) to obtain purified PLLA samples. The sample solution in the Petri dishes was placed in a chemical fume hood until the solvent evaporated completely and then was dried in a vacuum oven at 45 °C for 24 h. Ten milligrams of dried PLLA samples from each group were weighed for GPC testing.

After the preparation of all GPC samples, each PLLA sample was completely dissolved in 10 mL THF (tetrahydrofuran) at a concentration of 1 mg/mL. The solutions were transferred into GPC vials using a syringe with a 0.20 μm needle filter [31]. GPC analysis was performed on each sample category using a 100 μL injection volume at a flow rate of 1 mL/min with a refractive index (RI) detector at 40 °C using a TSKgel GMH_{HR}-M column. Results data were analyzed using Agilent GPC/SEC software (A.02.02) to calculate the average M_w, M_p, M_n, and $Đ_M$ for each sample category [83].

2.8. Surface and Cross-Sectional Surface Morphology

A digital optical microscope (Nikon Shuttle Pix P-400R, Nikon Corporation, Tokyo, Japan) was used to observe the surface appearance, morphology, and transparency of monofilaments at different degradation periods at magnifications of 120× to 200× [69].

To observe the effect of long-term degradation on iron wire-reinforced PLLA composite samples, micrographs of the surfaces and fractured cross-sectional surfaces of representative monofilaments were obtained using a Mira scanning electron microscope (SEM) (Tescan Mira 3, Oxford Instruments, Cambridge, UK) equipped with energy dispersive X-ray spectroscopy (EDS). The specimens were coated with a thin conductive gold layer using a Baltec SCD 005 sputter coater (BAL-TEC GmbH, Schalksmühle, Germany) at 0.13 mbar vacuum [84]. SEM images were acquired at magnifications of 150× and 250× using an acceleration voltage of 10.0 kV.

2.9. Differential Scanning Calorimetry

Differential scanning calorimetry (DSC) tests were performed using a Perkin Elmer Pyris 6 DSC (PerkinElmer, Inc., Norwalk, CT, USA) instrument to determine the thermal properties of in vitro-degraded PLLA and PLLA/Fe wire composite samples. A nitrogen gas flow rate of 30 mL/min was used to prevent oxidation. Samples (7–10 mg) were placed in non-perforated aluminum pans, which were crimped before testing. An empty crimped aluminum pan was used as the reference cell. The samples were first heated from 20 °C to 200 °C at a rate of 10 °C/min and held for 3 min. They were then cooled down to 20 °C at a rate of 10 °C/min and held for 3 min. A second heating scan was performed from 20 °C to 200 °C at a rate of 5 °C/min and held for 3 min. Finally, the samples were rapidly cooled down to 20 °C at a cooling rate of 50 °C/min. The glass transition temperature (T_g), cold crystallization temperature (T_{cc}), melting temperature (T_m), enthalpy of melting (ΔH_m), and enthalpy of crystallization (ΔH_c) of each sample were analyzed based on ISO standard 11357-2 2020 [85]. The T_g values were determined using the half-height method, while the T_m and T_{cc} values were identified based on their corresponding peak temperatures. The degrees of crystallinity (X_c) of PLLA samples were calculated using Equation (2):

$$X_c\ (\%) = (\Delta H_m - \Delta H_{cc})/(\omega \times \Delta H_m{}^0) \times 100\% \quad (2)$$

where ΔH_m (J/g) and ΔH_{cc} (J/g) are the melting enthalpy and cold crystallization enthalpy of tested PLLA samples, respectively; $\Delta H_m{}^0$ (J/g) is the melting enthalpy of com-

pletely crystalline PLLA (93.7 J/g) [70]; and ω is the weight fraction of PLLA in the PLLA/Fe composites [84,86,87].

$$\omega = (\rho_P \times (S_P - S_F))/(\rho_P \times (S_P - S_F) + \rho_F \times S_F) \quad (3)$$

where ρ_P and ρ_F are the densities of pure PLLA (1.24 g/cm^3) and iron wire (7.87 g/cm^3), respectively, and S_P and S_F are the cross-sectional areas of PLLA monofilament (1.8×10^{-3} cm^2) and Fe wire (3.32×10^{-5} cm^2), respectively. Therefore, the ω of PLLA in PLLA/Fe wire monofilament was 89.35% in this study.

2.10. Statistical Analysis

Statistical analyses were performed on the results using an independent-samples *t*-Tests to determine differences between PLLA and PLLA/Fe composite samples, while one-way analysis of variance (ANOVA) with a Tukey post-hoc test was used to determine the differences among different groups of the same type of samples [88]. Differences were considered significant at $p < 0.05$, $p < 0.01$, and $p < 0.001$, denoted as '*', '**', or '***', respectively [89]. SPSS (IBM version 29) software for Windows was used to perform these statistical analyses [80]. Data from mass loss and tensile tests collected in this study were expressed as mean ± standard deviation. A sample size of at least 3 was used for both tensile test and mass loss results.

3. Results and Discussion

3.1. Mass Change and Acceleration Mechanism of PLLA Matrix

3.1.1. Mass Change

As shown in Figure 3a, the mass loss of both 3D-printed PLLA/Fe wire and PLLA monofilaments increased gradually over the weeks of in vitro degradation. Overall, the mass losses of PLLA/Fe wire monofilaments were greater than those of PLLA samples over the same degradation periods, with significant differences observed in weeks 2 and 3. This suggests that the degradation rate of PLLA/Fe wire monofilaments was higher than that of PLLA monofilaments. Notably, at week 12, the mass loss percentage of the PLLA/Fe wire sample reached 17.56%, which was 3.8 times higher than that of the PLLA monofilament (4.63%). This accelerated degradation can be attributed to the enhanced corrosion of the iron wire in the local acidic regions of the degrading PLLA matrix, as some studies have indicated that iron corrosion can be accelerated by the acidic by-products of polymer hydrolysis [3,14,16,90–92]. Additionally, the pure PLLA samples exhibited a mass increase at the first collection point (week 1), while all other groups experienced mass losses. It should be noted that the mass changes for samples from weeks 8 and 10 were excluded due to some debris or fragment losses during cleaning and tensile testing operations. In contrast, the week 12 samples showed minimal debris loss because they were cleaned as a whole and did not undergo tensile testing prior to mass loss evaluation due to their curled state. Therefore, the mass losses for the week 12 samples were the average mass values of their entire individual groups. Remarkably, the mass loss percentages of both PLLA/Fe wire and PLLA monofilaments were below 2.5% during the first 6 weeks, equivalent to 6 months at body temperature (37 °C), with no significant differences between the sample categories, which is well in line with the previous studies (<3%) on PLLA monofilaments [93,94]. However, mass losses increased significantly in the later stages. These mass loss trends are consistent with findings from other recent studies [70,71,95,96]. Generally, the hydrolysis of PLLA begins in the amorphous regions, and mass loss occurs as short chains or monomers of PLLA molecules diffuse into the degradation solution [97]. In the early stages of degradation in this study, the diffusion of short chains or monomers was limited due

to the integrity of the PLLA microstructure and the high proportion of crystalline regions, as revealed by DSC results [70]. In the later stages, significant voids formed due to the degradation of amorphous regions, and more hydrolysis occurred in the crystalline regions, which constituted the main phase of the immersed samples. Consequently, mass losses became more pronounced from weeks 8 to 12.

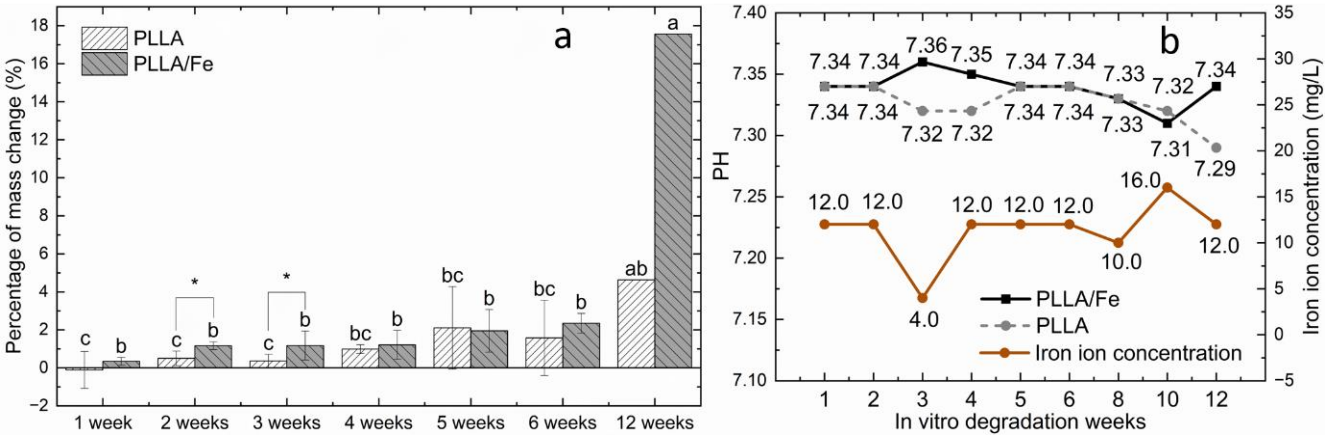


Figure 3. Mass changes (**a**) of in vitro-degraded PLLA/Fe wire and PLLA monofilaments, and the pH values (**b**) and iron ion concentrations of in vitro degradation solutions at the final sample collection time (week 12). Significant differences ($p < 0.05$) are denoted with an asterisk (*), while any two columns from one of the same material categories marked with at least one same lowercase letter (a, b, or c) indicate no significant difference.

3.1.2. Mechanism of Accelerated Degradation of Iron by PLLA Matrix

In recent years, several scientific studies have revealed the acceleration mechanism of PLA on iron bioresorbable materials [16,27,34,36,37,98]. As reported by Qi et al. [16], iron corrosion is primarily accelerated by the PLA matrix through lower local pH sites at the interface between the metal and polymer and the formation of a passive layer on the bare iron surface. The related acceleration mechanisms are explained below:

In the in vitro SBF degradation environment, pure Fe corrodes through the following reactions (4) and (5) [16]:

$$\text{Anodic reaction: } Fe \rightarrow Fe^{2+} + 2e^{-} \quad (4)$$

$$\text{Cathodic reaction: } O_2 + 2H_2O + 4e^{-} \rightarrow 4OH^{-} \quad (5)$$

Subsequently, Fe^{2+} reacts with hydroxide ions to form ferrous hydroxide ($Fe(OH)_2$). However, this corrosion product can further convert into ferric hydroxide ($Fe(OH)_3$) on the bare iron wire and the surrounding PLLA surface, even under weakly alkaline or low-oxygen conditions. These corrosion products may then combine with ions (CO_3^{2-}, Cl^{-}, and SO_4^{2-}) from the SBF solution to form green rust on the iron wire and surrounding PLLA surface [98], as observed in Figure 4. At later stages, this green rust converts into a black, insoluble compound, similar to the by-products attached to the samples, especially in the 12-week samples. Relevant reactions include [98]:

$$Fe^{2+} + 2OH^{-} \rightarrow Fe(OH)_2 \quad (6)$$

$$Fe(OH)_2 + OH^{-} \rightarrow Fe(OH)_3 + e^{-} \quad (7)$$

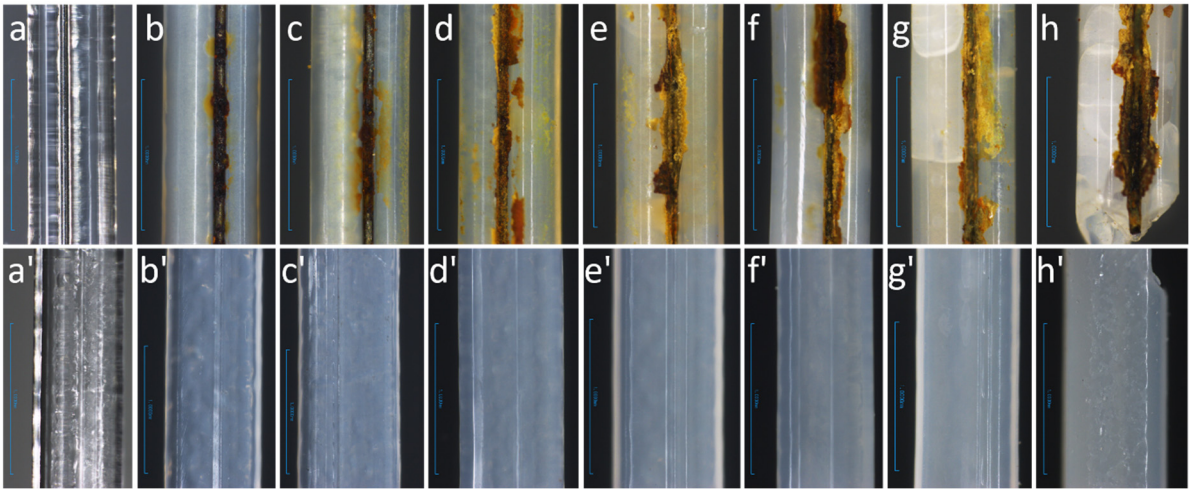


Figure 4. Optical images of outer surfaces of PLLA/Fe wire and PLLA monofilaments: (**a**–**h**) and (**a′**–**h′**) for PLLA/Fe wire and pure PLLA samples of weeks 0, 1, 2, 4, 6, 8, 10, and 12, respectively.

In an aqueous environment, PLLA undergoes hydrolytic degradation. The polyester chains break down into carboxyl-terminated and hydroxyl-terminated chains as water molecules diffuse into the PLLA matrix during degradation, as shown in the following reaction (8) [34]:

$$\text{Poly}_1\text{–COO–Poly}_2 + \text{H}_2\text{O} \rightarrow \text{Poly}_1\text{–COOH} + \text{Poly}_2\text{–OH} \quad (8)$$

Among the degradation products, the carboxyl end groups exhibit acidic properties, contributing to locally reduced pH sites around the sample surface [98]. Under these acidic conditions, iron corrosion by-products such as ferrous and ferric hydroxide can dissolve into iron ions in the SBF solution, which further prevents the formation of passive layers on the iron surface. This allows more of the iron wire to remain exposed to both oxygen and the acidic environment, which promotes the degradation rate of iron.

3.2. PH and Iron Ion Concentration

The pH of the degradation solutions for both PLLA/Fe wire and PLLA monofilaments showed a slightly decreasing trend over the 12-week degradation period, with all pH values remaining between 7.29 and 7.36. This is consistent with the pH results of PLLA stents immersed in PBS at 50 °C for 4 months, as reported in a 2023 study [99]. In contrast, some in vitro degradation studies on PLLA samples have shown a more pronounced decrease in pH during degradation [22,81,100,101]. At most time points, the PLLA/Fe degradation solution showed similar PH values to those of PLLA samples. The relatively minor pH variations and similarities observed in this study could be due to the high sample-to-SBF ratio, combined with the buffering capacity of tris(hydroxymethyl)aminomethane present in the SBF [34]. Only at three testing points (weeks 3, 4, and 12) were the pH values of the PLLA/Fe degradation solutions slightly higher than those of neat PLLA solutions, as shown in Figure 3b. This could indicate that the corrosion of the iron wire in the PLLA matrix exerted a certain degree of neutralizing effect on the acidic by-products of PLLA degradation, such as lactic acid. This neutralizing interaction between the degradation by-products of bioresorbable metals and aliphatic polyesters like PLA has been demonstrated in several recent studies [29–35]. The alkaline by-products of iron wire corrosion, including $Fe(OH)_2$ and $Fe(OH)_3$, may help mitigate inflammatory reactions as reported in some studies [3,27,34,102] caused by the acidic degradation products of PLLA [22,93].

For the iron ion concentration of the PLLA/Fe degradation solutions, it can be seen that the trend of released iron ions is consistent with that of the pH values. When the pH is higher than the average value, the iron ion concentration is lower at the 3-week degradation point. Conversely, a higher iron ion concentration corresponds to a lower pH value at the testing point of week 10. This observation is reasonable, considering that most of the corroded iron by-products exhibit low solubility in mildly alkaline SBF and tend to adhere to the surface of the iron wire and the surrounding PLLA matrix [27]. This can be confirmed by the surface images of the PLLA/Fe samples shown in Figure 4. When the pH is lower, more iron ions can be released into the degradation solution, whereas higher pH values suppress iron ion release [16,37]. Another possible reason for the mild variation in iron ion concentration throughout the degradation period is the high sample-to-SBF ratio, as discussed in the pH results.

3.3. GPC Analysis

The average molecular weights of polymeric materials are crucial chemical properties that determine their physical performance, including mechanical properties (strength, modulus, stiffness, strain, etc.), thermal properties (melting temperature, glass transition temperature, crystallinity degree, etc.), appearance (cracks, transparency, etc.), viscosity, and more [65,103]. The comparison of molecular weights (including M_w, M_n, M_p, and $Đ_M$) between PLLA/Fe wire and PLLA monofilaments is presented in Figure 5. The average molecular weights of degraded PLLA samples from both types of monofilaments gradually decreased over the degradation period. Specifically, the PLLA filament samples showed reductions from 69.12 to 6.69 kDa in M_w, 17.43 to 2.30 kDa in M_n, and 50.73 to 3.07 kDa in M_p. Meanwhile, the PLLA/Fe filament samples decreased from 64.05 to 8.42 kDa in Mw, 16.16 to 2.33 kDa in Mn, and 50.44 to 3.04 kDa in M_p. By week 12, the average molecular weights of both types of monofilaments were nearly identical, with reductions of approximately 85–90% for M_w and M_n and 94% for M_p by week 12, equivalent to 12 months at body temperature (37 °C). These reductions in molecular weights are consistent with findings (M_w: 92% and M_n: 93%) from a previous study conducted at 37 °C for 12 months [70]. Notably, there were no significant differences (all $p > 0.05$) in M_w, M_n, and M_p values between the PLLA and PLLA/Fe samples at all degradation weeks according to *t*-Test statistic results, as shown in Table 6, which suggests that the embedded iron wire did not accelerate the degradation rate of PLLA samples by the end of the in vitro degradation period at 50 °C.

In addition, the polymer dispersity ($Đ_M$) values of PLLA filaments exhibited mild decreases from 4.58 to 2.97, and PLLA/Fe counterparts exhibited relatively stable values. No significant differences were found within both sample groups, and there were no significant differences among the two types of samples at the same degradation point, as shown in Figure 5d and Table 6.

Table 6. The *t*-test *p* values for the molecular weight comparisons between degraded PLLA and PLLA/Fe filaments.

	Week 0	**Week 2**	**Week 4**	**Week 6**	**Week 8**	**Week 12**
M_w	0.71	0.10	0.68	0.39	0.36	0.18
M_n	0.86	0.96	0.89	0.49	0.75	0.93
M_p	0.98	0.58	0.29	0.33	0.55	0.84
$Đ_M$	0.61	0.74	0.73	0.76	0.36	0.38

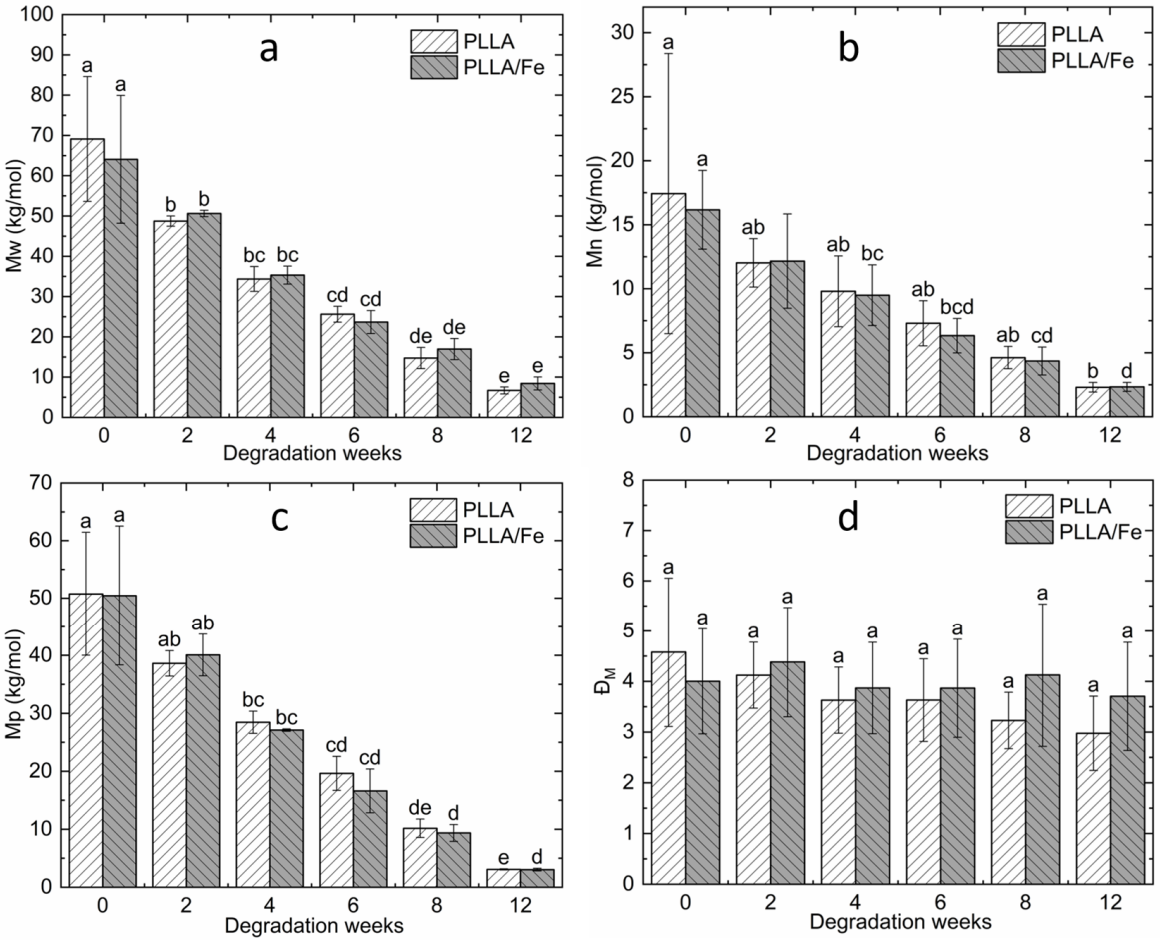


Figure 5. GPC results of 3D-printed and in vitro-degraded PLLA/Fe and PLLA monofilaments: (**a**) weight-average molecular weight, (**b**) number-average molecular weight, (**c**) peak molecular weight, and (**d**) dispersity. Any two columns from one of the same material categories marked with at least one same lowercase letter (a, b, c, d, or e) indicate no significant difference ($p < 0.05$).

3.4. DSC Analysis

The DSC results from two heating scans are presented in Figures 6 and 7, illustrating the thermal behaviors of both original extruded and in vitro-degraded PLLA/Fe and PLLA monofilament samples. As shown in Figure 6a–d, the heat flow curves of PLLA/Fe and PLLA samples demonstrated similar trends in typical thermal properties. Notably, T_{cc} peaks were absent in the in vitro-degraded samples but were prominent in the original printed samples. This is also observed in DSC curves of PLLA monofilaments degraded at 60 °C in Shi et al.'s study [93]. The absence of T_{cc} peaks in both types of degraded samples indicates that both samples immersed in SBF at 50 °C underwent significant recrystallization during their degradation periods. As shown in Figure 6e,f, a remarkable finding was that the crystallinity (X_c) of both samples increased sharply to around 75% by week 2 and then gradually rose to around 95% by week 8, with slight decreases observed after week 8. This significant increase in X_c for semi-crystalline polymers is known as degradation-induced recrystallization and is also observed in the X_c results (10% to 37%) of Zhao's study [70]. The sharp initial increase is attributed to the formation of new crystals, as molecular chains in amorphous regions have higher mobility at 50 °C than at room temperature [104]. The subsequent gradual increase is due to the realignment of shorter polymer chains produced by chain scission during degradation [77]. The decrease in X_c at the later stages is caused by chain breaks in the crystalline regions of PLLA samples following the hydrolysis of a large proportion of amorphous phases, as reported in relevant

studies [77,99]. The X_c of the original PLLA/Fe wire samples (7.88%) was higher than that of the PLLA counterparts (2.24%), likely due to the nucleating effect of the embedded iron wire and the residual heat from the iron wire after coextrusion. The rapid and significant increase in X_c for both samples is also attributed to the degradation test temperature (50 °C), as observed in previous studies [105]. While X_c increases have also been reported in other in vitro degradation studies at 37 °C, the effect of the elevated degradation temperature of 50 °C on the performance of biodegradable medical devices warrants further investigation.

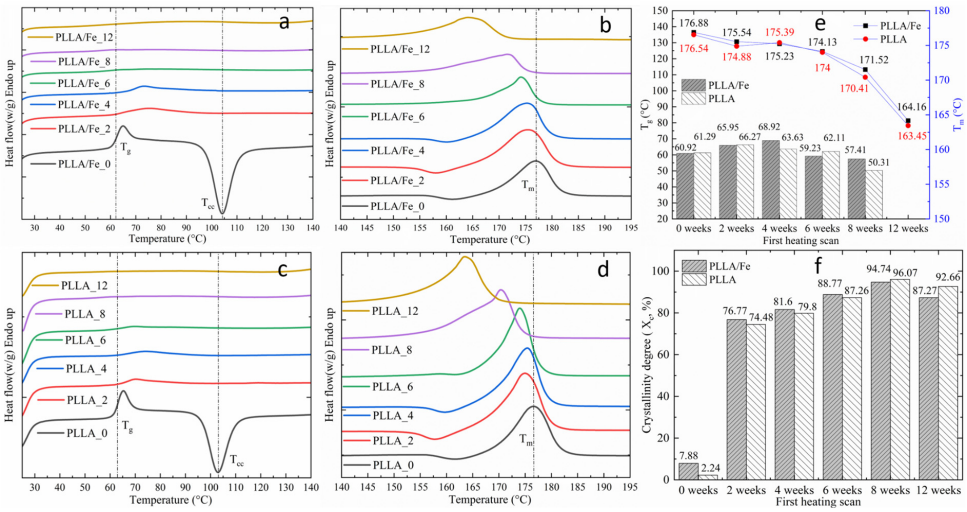


Figure 6. The first heating scan curves of PLLA/Fe wire (**a**,**b**) and PLLA (**c**,**d**) monofilaments, along with their corresponding Tg and Tm (**e**) and Xc (**f**) results.

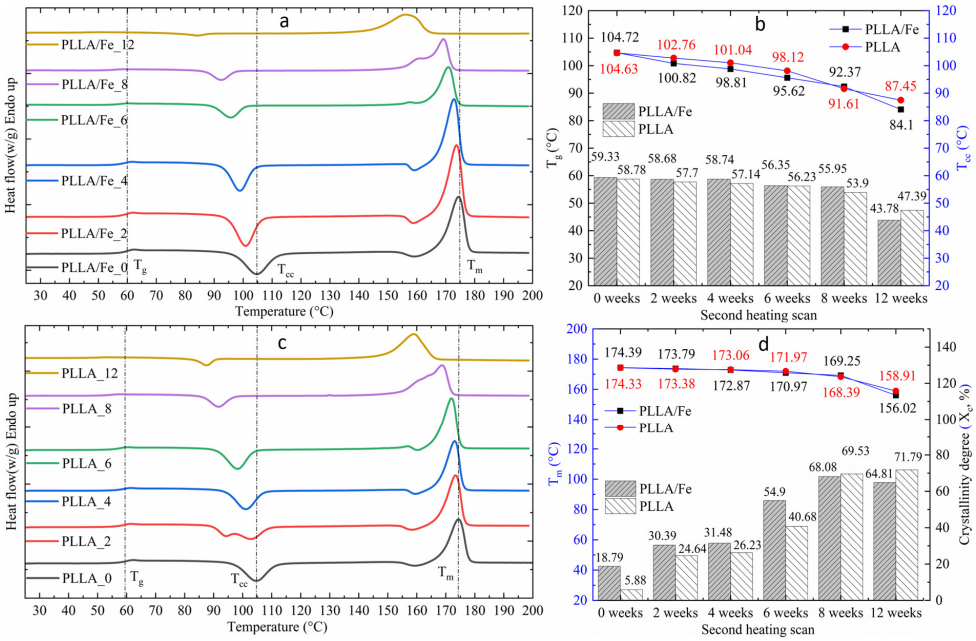


Figure 7. The second heating scan curves of PLLA/Fe wire (**a**) and PLLA (**c**) monofilaments, along with their corresponding T_g and T_{cc} (**b**) and T_m and X_c (**d**) results.

Generally, the T_g of PLLA decreases with its molecular weight. In this study, the T_g (around 60 °C) of both samples increased until week 4 and then gradually decreased to 57.41 °C (PLLA/Fe_12) and 50.31 °C (PLLA_12) by week 12. This trend, also observed in Moetazedian et al.'s study [104], can be explained by the dominant effect of increasing X_c in the first 4 weeks, followed by the dominant effect of molecular weight reduction [77]. Furthermore, the T_m values of both samples decreased gradually during the first 6 weeks

and reached 164.16 °C (PLLA/Fe_12) and 163.45 °C (PLLA_12) by week 12, consistent with their trends in molecular weights and mass losses. The compensation effect of the significant increase in X_c also influenced the slower reductions in T_m at the early stages. Despite similar trends, the PLLA/Fe samples exhibited slightly higher T_m values than the PLLA samples, as shown in Figure 6e.

In the second heating scan, after eliminating thermal history effects, the thermal properties of both sample types exhibited more uniform gradient changes, as shown in Figure 7b,d. A notable difference from the first heating scan was the presence of T_{cc} peaks in the DSC curves of the degraded samples (Figure 7a,c), which is typical behavior for PLA samples without the influence of elevated temperature (50 °C) degradation. The key thermal properties, including T_g, T_{cc}, and T_m, of both samples in the second heating scan showed consistent and gradual decreases over the degradation period, aligning closely with their trend of reduced molecular weights. Additionally, these properties exhibited relatively strong decreases between weeks 10 and 12, suggesting slightly faster degradation rates in the later stages. In terms of comparison, the T_g values of PLLA/Fe samples were slightly higher than those of PLLA filaments, while the PLLA samples showed marginally higher T_{cc} values in the first 8 weeks. Regarding X_c, the PLLA/Fe samples exhibited higher X_c values than the PLLA filaments during the first 6 weeks of degradation, with both types showing gradual increases in X_c over the degradation weeks. This trend was also reported in Chausse et al.'s study (X_c_PLLA: 27.2–51.5%) [99]. Furthermore, there was little difference in T_m values between the two sample types from week 0 to 6, likely due to the combined effects of the relatively higher molecular weights of PLLA samples and the higher X_c values of PLLA/Fe samples [97]. The slight difference in T_m values between the two types of PLLA samples at week 12 was primarily due to the difference in X_c values, as their molecular weights were nearly identical by that point.

Generally, the degree of crystallinity plays an important role in the degradation rate and mechanical properties of semi-crystalline polymers [106], with higher X_c values associated with a lower hydrolysis degradation rate and better mechanical performance [103]. The unexpectedly high crystallinity degrees of both samples after immersion could have exerted an impediment effect on their mass losses until the late stage, as indicated by the mass change results discussed above. Moreover, an increase in X_c for semi-crystalline polymers typically results in a higher Young's modulus, stiffness, and strength [77,97]. The relevant discussion is provided in the tensile test section of this study.

3.5. Sample Appearance and Morphology

The optical appearances and SEM images of the original and degraded PLLA/Fe and PLLA monofilaments are presented in Figures 4 and 8. Both initial printed PLLA/Fe and PLLA monofilaments had a transparent, glassy appearance, but the transparency of both degraded samples gradually decreased over the degradation weeks. Similar appearance changes have been reported in recent studies [70,104]. Notably, both samples became noticeably opaque after 1 week of degradation, consistent with the increases in X_c values during degradation discussed earlier. Additionally, the PLLA/Fe samples appeared slightly more opaque than the corresponding PLLA samples, aligning with the slightly higher X_c values of PLLA/Fe samples in the first 6 weeks, as shown in Figure 4f. Despite the differences in transparency, samples from week 0 to week 8 exhibited similar microstructures, with smooth surfaces and no visible voids or pits, consistent with findings from existing studies [70,94]. However, cracks or similar crack-like features can be seen in both optical images (Figure 4h,h′) and SEM images (Figure 8f,f′,l,l′) of both week_12 samples, indicating significant destructive degradation. This observation aligns with the mass losses observed in the later stages. Cracks were also visible in the appearance images of the week

8 samples, and tensile tests could not be performed on either type of sample degraded for more than 6 months due to their fragility. These cracks are likely caused by the severe hydrolysis of amorphous regions between crystalline regions [99]. On the other hand, the iron wire embedded in the PLLA filament exhibited random corrosion during the first week of immersion, with more intensive corrosion occurring over subsequent weeks, as evidenced by the increasing presence of corrosion by-products containing Ca/P or passive layers around the iron wire (Figures 4b–h and 8b–f).

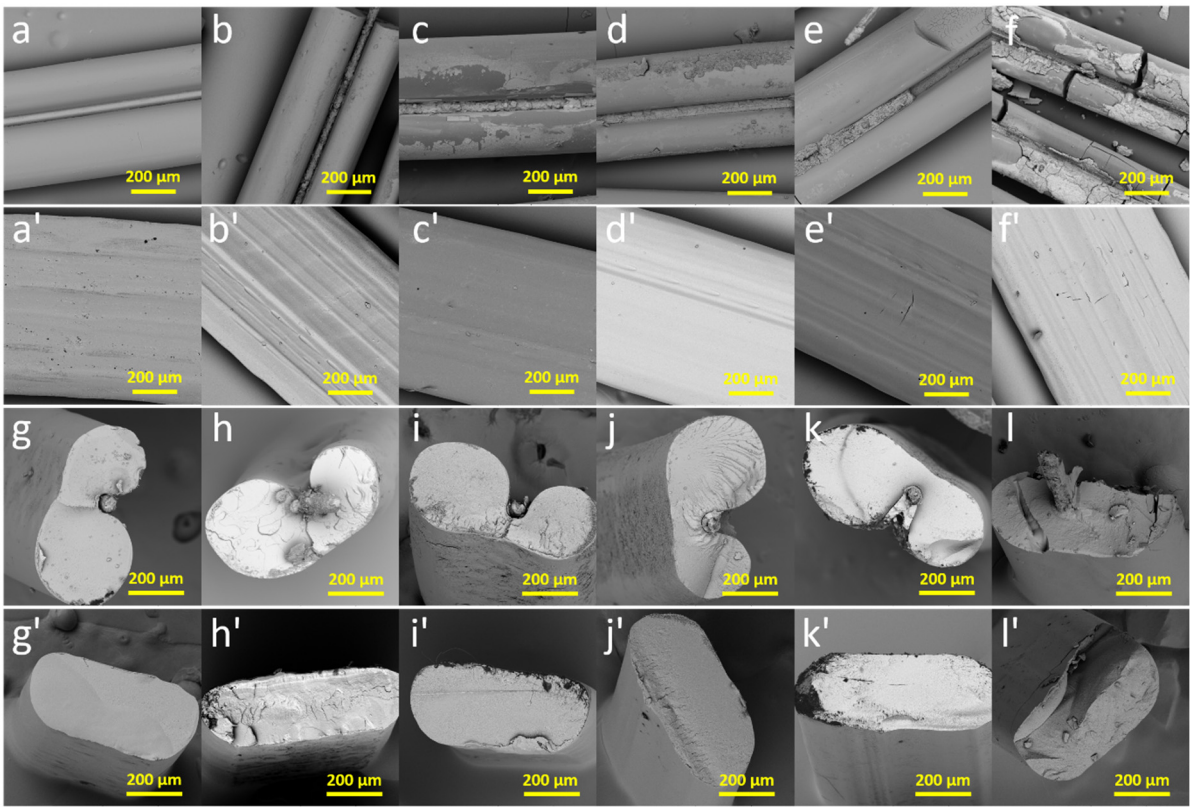


Figure 8. SEM images: the outer surface (**a**–**f**) and cross-sectional (**g**–**l**) surface appearances of PLLA/Fe samples, and the outer surface (**a′**–**f′**) and cross-sectional surface (**g′**–**l′**) appearances of PLLA samples for weeks 0, 2, 4, 6, 8, and 12, respectively. The scale bars in all images represent 200 μm.

Notably, the iron wires were not fully encapsulated by the PLLA matrix in all PLLA/Fe samples, despite being centrally positioned within the filaments, as observed in the cross-sectional images (Figure 8g–l). This unexpected embedding condition has also been reported in recent studies involving copper- or steel-embedded polymer specimens for applications such as mechanical testing, thermal conductivity enhancement, and sensing [56,61,107]. The mechanism underlying the poor top coverage of the PLLA matrix can be illustrated by the 3D schematic in Figure 9. During the PLLA/Fe coextrusion process, the iron wire is displaced from the nozzle's central axis (yellow dashed centerline in Figure 9b) and drawn toward the nozzle wall due to the drag force (F, as shown in Figure 9b) exerted by the previously extruded PLLA/Fe monofilament. Specifically, the portion of the iron wire in contact with the nozzle wall is not encapsulated by the PLLA melt due to the frictional interaction between the wire and the nozzle wall. Additionally, the iron wire may act as a splitting tool on the top surface of the extruded PLLA melt, as illustrated in Figure 9c.

The poor embedding quality resulted in premature corrosion of the iron wire, significantly weakening its reinforcement effect during the early stages (weeks 1–6) and

potentially exerting a negative impact on the mechanical strength of the PLLA/Fe wire monofilaments. Therefore, to ensure optimal reinforcement, the embedding and coverage quality of the iron wire within the PLLA matrix should be improved [56]. Improvement strategies can be derived from the underlying mechanism of poor iron wire coverage. One effective approach is to keep the iron wire aligned with the nozzle centerline by optimizing the nozzle design, for example, by incorporating a dedicated wire-guiding channel. Another method involves reducing the splitting effect of the iron wire and enhancing the adhesion of the PLLA melt to its surface through surface treatments such as micro-arc oxidation (MAO), sandblasting, acid etching, or the application of silane coupling agents [108]. Additionally, employing a secondary, smaller extrusion outlet along with the main nozzle outlet is recommended to address the poor surface coverage defect. Last but not least, a stronger yet thinner biodegradable metal wire should be used as the reinforcing element, as thinner wires are more easily encapsulated by the polymer matrix.

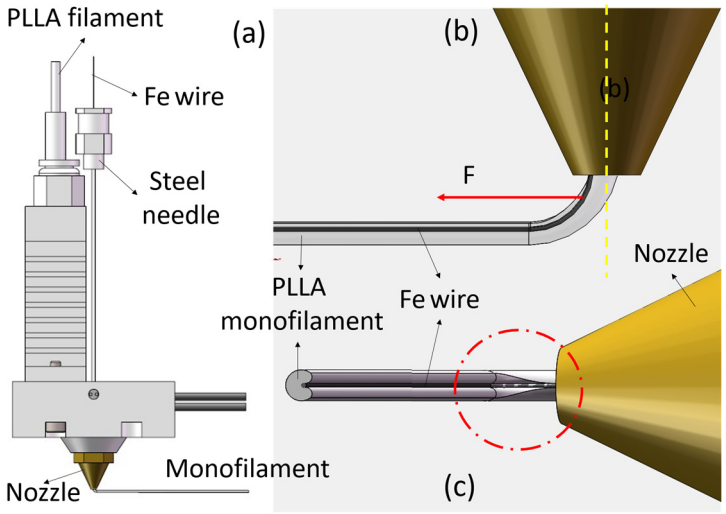


Figure 9. 3D diagram of PLLA/Fe coextrusion head (**a**) and iron embedding: front view (**b**) and top view (**c**).

Regarding the interfacial stability of PLLA/Fe wire monofilaments during the degradation period, it can be observed that the interface between PLLA and the iron wire did not exhibit signs of a loosening trend throughout the degradation period, as the interfacial gaps between the two materials did not increase over time, according to the PLLA/Fe sample images in Figure 8g–l. Notably, the interfaces between PLLA and Fe wire in the samples at weeks 6, 8, and 12 appeared smaller and more compact. Therefore, the coextrusion 3D-printed PLLA/Fe wire monofilaments demonstrated good interfacial stability during the in vitro degradation. Finally, it is worth noting that the circular cross-sections of the 3D-printed monofilaments can not only reduce the blood flow interface within vessels but also promote the recovery of normal endothelial function due to the absence of sharp transition corners compared to traditional stent filaments with rectangular cross-sections [2,109].

3.6. Tensile Properties

Before analyzing the tensile properties of the monofilaments, it should be noted that both PLLA and PLLA/Fe wire composite monofilaments degraded for more than 6 weeks (equivalently 6 months at 37 °C) were too fragile to be mounted in the grips without breaking. Similar fragility has been reported in previous studies for monofilaments prepared by melt spinning after 8 months of degradation at 37 °C [70,74,77,95]. The fragility of long-term degraded samples is attributed to the severe hydrolysis of PLLA chains in

amorphous regions, leading to weak bonding between crystalline regions [99,110], as indicated by the morphological observations discussed above.

The average Young's modulus, stiffness, tensile strength, and strain at maximum load of 3D-printed and degraded PLLA/Fe and PLLA monofilaments are shown in Figures 10 and 11. The embedding of iron wire effectively improved the Young's modulus and stiffness of PLLA monofilaments in the early stages (up to 4 weeks), which is beneficial for preventing stent recoil after implantation [5,26,111,112]. Significant differences were observed in weeks 0, 1, 2, and 4, highlighting the remarkable reinforcement effect of the iron wire. The maximum improvements due to the embedded iron wire were 52.16% for Young's modulus, 60.92% for stiffness, and 3.30% for tensile strength in the initial (week 0) samples. However, from week 5 onward, the PLLA monofilaments exhibited higher modulus and stiffness than the PLLA/Fe samples, likely due to severe localized corrosion at random positions on the embedded iron wire. Interestingly, the PLLA/Fe samples showed gradual decreases in the Young's modulus and stiffness over the degradation weeks, while the PLLA samples exhibited slight declines in the first two weeks and higher values from weeks 3 to 6. This trend aligns with the results of PLLA samples in previous studies [77,94]. The gradual decline in the PLLA/Fe samples is attributed to the loss of reinforcement from the iron wire, indicating that the embedded iron wire played a dominant role in the modulus and stiffness properties of the PLLA/Fe wire monofilaments. Meanwhile, unexpected variations in the modulus and stiffness values of PLLA monofilaments have also been reported in previous PLLA degradation studies [77,103,113–116]. Abaei et al. [97] suggested that changes in both crystallinity and molecular weights should be considered together to explain the elastic behavior of PLLA during degradation. At the early stages, the modulus and stiffness losses caused by molecular weight reduction were counterbalanced by increases in crystallinity, while the increases from weeks 3 to 6 were due to rising X_c values and the loss of elasticity caused by the gradual disappearance of amorphous regions of the PLLA monofilaments.

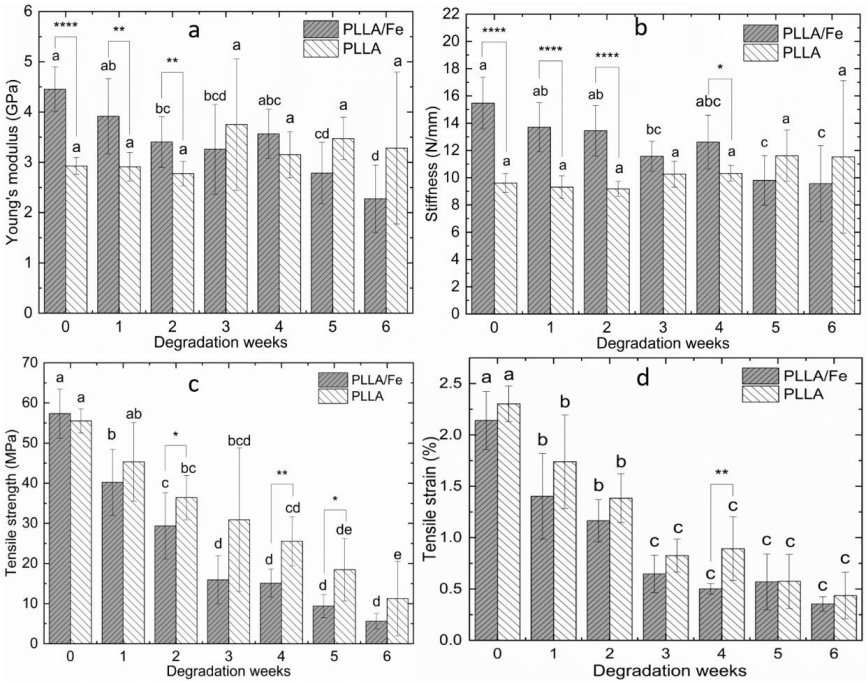


Figure 10. Mechanical properties of in vitro-degraded PLLA/Fe wire and PLLA monofilaments: (**a**) Young's modulus, (**b**) stiffness, (**c**) tensile strength, and (**d**) tensile strain. Significant differences are denoted with asterisks: '*' for $p < 0.05$, '**' for $p < 0.01$, and '****' for $p < 0.0001$. Any two columns from one of the same material categories marked with at least one same lowercase letter (a, b, c, d, or e) indicate no significant difference ($p < 0.05$).

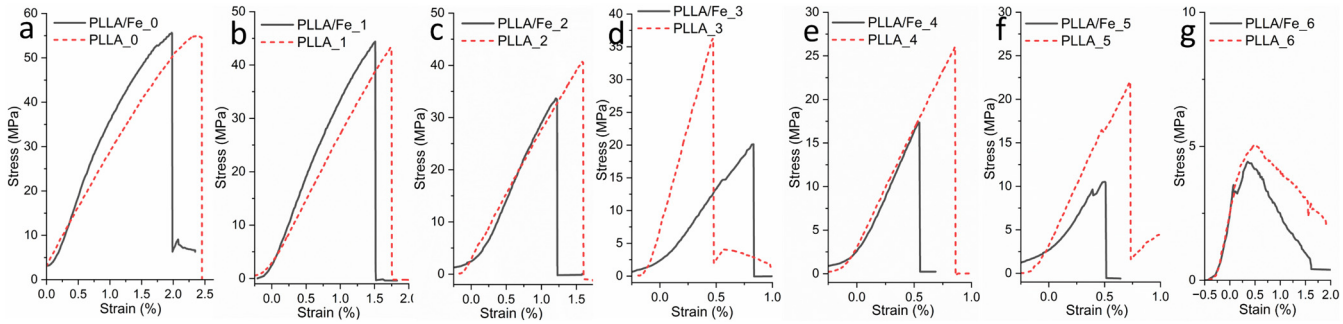


Figure 11. Representative stress–strain curves of tensile tests for monofilaments from week 0 to 6 (**a**–**g**).

One of the most evident conclusions is that both types of monofilaments exhibited gradual decreases in tensile strength and strain over the degradation weeks, consistent with the results of Weir et al. [71]. In contrast, a previous study has reported a smaller reduction (approximately 60%) in the tensile strength of PLLA samples over a degradation period of six months [70]. The gradual decrease in tensile strain for both sample types, as reported by Moetazedian et al. [104], can be explained by the increasing X_c values of both samples [97]. While the original printed PLLA/Fe wire monofilaments showed improved tensile strength compared to the PLLA samples, the tensile strengths of the degraded PLLA samples were higher than those of the PLLA/Fe counterparts. This suggests that the embedded iron wire negatively affected the tensile strength of the PLLA filaments during degradation, likely due to incomplete coverage of the iron wire by the polymer matrix, which led to severe and random corrosion. Therefore, improving the embedding quality of the iron wire within the PLLA matrix during 3D printing is essential to preventing early-stage corrosion and maintaining the reinforcement effect during the implantation period. If the iron wire is well-centered and fully covered by the PLLA matrix, the thicker PLLA outer layer can protect the iron wire from severe corrosion in the early stages, as demonstrated by Qi et al. [36,98]. This would ensure sufficient Young's modulus, stiffness, and tensile strength to meet the radial force requirements of arterial stents during the early stages of implantation. Notably, the PLLA samples exhibited higher strain values than the PLLA/Fe counterparts, as evident in the tensile stress–strain curves shown in Figure 11a–g. The lower average tensile strain of the PLLA/Fe monofilaments indicates that the embedded iron wire improved the modulus but reduced ductility.

In addition, the tensile strength of the virgin PLLA/Fe wire monofilaments at week 0 (57.33 ± 6.12 MPa) was significantly lower than the benchmark value for vascular stents (~300 MPa), as reported in previous studies [117,118]. One of the primary reasons for this low strength is the use of relatively weak and low-cost materials, PLLA (~50 MPa) and iron wire (180–210 MPa), in this early-stage study. In contrast, the tensile strength of stent-grade-oriented PLLA typically ranges from 100 to 150 MPa, and the iron wire used here also shows lower tensile strength compared to the iron materials commonly employed in conventional iron alloy stents [119]. Therefore, one of the strategies to improve the mechanical performance is to adopt higher-strength PLLA filaments and biodegradable metallic alloy wires. The second approach is to improve the embedding quality of the iron wire within the PLLA matrix, as this directly affects the mechanical performance of the printed PLLA/Fe monofilaments. Improvement measures include the use of higher-quality 3D printers, dedicated nozzle design, and a second small extrusion outlet to improve the embedding quality of iron wire, as discussed in the section above. Thirdly, surface treatments like Micro-Arc Oxidation (MAO), sandblasting, acid etching, silane coupling agents, etc., can be applied to the iron wire surface to enhance the interface adhesion

strength between the PLLA matrix and iron wire significantly [108]. Therefore, there is great improvement space for the mechanical performance of printed metallic wire-reinforced PLLA monofilaments in future studies.

Although the tensile strength improvement was not significant, the embedded iron and its corrosion by-products (e.g., iron oxides) can enhance the radiopacity of PLLA monofilaments for stents [19,120–122]. Radiopacity is a critical feature for ideal stents, as the low density of PLLA makes it insufficient for medical imaging techniques such as CT and MRI [3,9,123].

4. Conclusions

The current work is the first study to report the in vitro-accelerated degradation profile of continuous iron wire-reinforced PLLA monofilaments fabricated using a novel 3D printer for the development of bioresorbable vascular stents. The PLLA/Fe wire composite is expected to be a promising biodegradable material for stent applications, as this polymer–metal composite could potentially combine the accelerating effect of PLLA hydrolysis on iron corrosion with the excellent mechanical strength of the iron component. Based on the 12-week in vitro dynamic degradation study at 50 °C, several promising and notable conclusions were obtained, as follows:

Firstly, this work demonstrated the feasibility of fabricating continuous iron wire-reinforced PLLA monofilaments using a novel 3D printer, which was modified from an open-source 3D printer at a low cost. Secondly, while previous studies confirmed that the in vitro degradation of iron can be accelerated by aliphatic polyesters such as PLA, PLGA, and PGA, this study revealed that the embedding of iron wire did not accelerate or reduce the degradation rate of the PLLA matrix in SBF solution at 50 °C, as the molecular weights of neat PLLA monofilaments (M_w: 6.2 kDa, M_n: 2.73 kDa, and M_p: 3.2 kDa) were similar to those of PLLA/Fe wire monofilament samples (M_w: 6.9 kDa, M_n: 2.73 kDa, and M_p: 3.3 kDa) at week 12, the final degradation week. Notably, the overall degradation rate of PLLA/Fe wire monofilaments was accelerated compared to that of PLLA monofilaments since the mass loss percentage of the PLLA/Fe wire sample reached 17.56%, which was 3.8 times higher than that of the PLLA monofilament (4.63%) at week 12. Thirdly, PLLA samples from both degraded PLLA/Fe wire and neat PLLA monofilaments exhibited similar values and trends in both the first and second heating scans. Furthermore, both samples showed sharp increases (from 7.88% and 2.24% at week 0 to 76.77% and 74.48% at week 1 for PLLA/Fe and neat PLLA, respectively) in X_c after one week of degradation and increasing drop rates in T_m in the first heating scan. Meanwhile, all thermal properties exhibited gradual decreases in T_g, T_{cc}, and T_m, and gradual increases in X_c with the gradual decreases in molecular weights in the second heating scan. Notably, the Young's modulus and stiffness of the PLLA/Fe wire monofilaments were significantly improved by the incorporation of iron wire prior to the fourth week of degradation, with Young's modulus values of 4.45 GPa and 3.40 GPa, and stiffness values of 15.47 N/mm and 13.45 N/mm, for PLLA/Fe wire samples at weeks 0 and 3, respectively. In contrast, the PLLA samples exhibited Young's modulus values of 2.93 GPa and 2.76 GPa, and stiffness values of 9.61 N/mm and 9.17 N/mm, at the corresponding time points. However, the reinforcement effect of the iron wire on tensile strength became negative after immersion due to severe random localized corrosion at the early stage, caused by the poor embedding quality of the iron wire in the PLLA matrix.

Overall, this is the first study to demonstrate the feasibility of fabricating continuous iron wire-reinforced PLLA monofilaments using a custom-built polymer filament–metal wire coextrusion 3D printer. This lays the foundation for further development of metal wire-reinforced polymer vascular stents by integrating the novel coextrusion process with a

rotating mandrel-assisted 3D printing technique. Moreover, the 3D-printed PLLA/Fe wire monofilaments exhibited better performance in Young's modulus and stiffness, and a higher overall degradation rate compared to neat PLLA counterparts, indicating the reinforcement of the embedded iron wire. Improved performance and deeper insights are expected if the embedding quality of the iron wire within the PLLA matrix can be improved in future studies. Finally, this early-stage prototype study presents a promising and practical approach for developing continuous metal wire-reinforced polymer composites for a range of biomedical applications, including esophageal stents, tracheal stents, and bone scaffolds, among others.

5. Limitations and Future Work

This study has provided valuable insights into the in vitro-accelerated degradation profile of 3D-printed continuous iron wire-reinforced PLLA monofilaments for vascular stent development. However, several limitations need to be addressed in future research. Firstly, the thermally accelerated degradation period should be extended from 3 months to one year or more to fully understand the degradation behavior of PLLA/Fe samples at later stages until complete absorption, since the samples at week 12 were still far from complete degradation. Additionally, monitoring the iron ion concentration in the degradation solution over time would provide more direct data on the corrosion rate of the iron wire, offering a clearer picture of its degradation kinetics. Furthermore, the embedding quality of the iron wire within the PLLA monofilaments needs to be improved to ensure uniform and complete coverage, which is critical for obtaining more valuable and reproducible results for the development of bioresorbable PLLA/Fe wire composite stents.

To advance this research, future work should focus on several areas, as indicated below. First, the embedding quality of the continuous iron wire in the PLLA matrix during 3D printing should be enhanced, potentially by optimizing the polymer–metal coextrusion head. This would help prevent random corrosion of the iron wire at early degradation stages, maintaining enough iron reinforcement for the vascular remodeling at early stages. Second, the 3D printing process should be optimized to fabricate PLLA/Fe wire monofilaments with a thickness of between 100 and 150 μm, which is critical for the development of vascular stents. Achieving this would require careful optimization of printing parameters and the novel polymer filament–metal wire coextrusion head. Addressing these limitations and recommendations will contribute to the development of bioresorbable PLLA/Fe composite stents based on 3D printing technology. Last but not least, with the improvement of this novel process, further studies can be extended to other promising applications, including bone scaffolds and 3D printing of shape memory materials, among others.

Author Contributions: Conceptualization, H.L. and Y.C.; methodology, H.L., A.P., Y.L., D.P.F. and G.Y.; software, K.G.; validation, H.L. and A.P.; formal analysis, H.L. and H.X.; investigation, H.L., A.P., Y.L., G.Y., V.C. and D.P.F.; resources, A.P., V.C. and K.G.; data curation, H.L.; writing—original draft preparation, H.L.; writing—review and editing, H.L. and Y.C.; visualization, H.L. and H.X.; supervision, R.D. and Y.C.; project administration, H.L. and Y.C.; funding acquisition, Y.C. and H.L. All authors have read and agreed to the published version of the manuscript.

Funding: This research was funded by the Science Foundation of Ireland (Grant number: SFI 18/IF/6248), and the President's Doctoral Scholarship Fund (Fund number: PA00005) from the Technological University of the Shannon: Midlands Midwest, Ireland.

Data Availability Statement: Data will be made available on request.

Conflicts of Interest: The authors declare no conflicts of interest.

References

1. Yuan, Y.; Jin, X.; Fan, Z.; Li, S.; Lu, Z. In Vivo Degradation of Copolymers Prepared from L-Lactide, 1,3-Trimethylene Carbonate and Glycolide as Coronary Stent Materials. *J. Mater. Sci. Mater. Med.* **2015**, *26*, 139. [CrossRef]
2. Toong, D.W.Y.; Ng, J.C.K.; Cui, F.; Leo, H.L.; Zhong, L.; Lian, S.S.; Venkatraman, S.; Tan, L.P.; Huang, Y.Y.; Ang, H.Y. Nanoparticles-Reinforced Poly-l-Lactic Acid Composite Materials as Bioresorbable Scaffold Candidates for Coronary Stents: Insights from Mechanical and Finite Element Analysis. *J. Mech. Behav. Biomed. Mater.* **2022**, *125*, 104977. [CrossRef] [PubMed]
3. Gąsior, G.; Szczepański, J.; Radtke, A. Biodegradable Iron-Based Materials—What Was Done and What More Can Be Done? *Materials* **2021**, *14*, 3381. [CrossRef] [PubMed]
4. Zhang, Y.; Du, H.; Qiu, Z.; Liu, W.; Hu, Y.; Wang, C.; Ding, J. Enhancement of Poly-L-Lactic Acid Stents through Polydopamine Coating: Boosting Endothelialization and Suppressing Inflammation. *Alex. Eng. J.* **2023**, *81*, 525–531. [CrossRef]
5. Im, S.H.; Jung, Y.; Kim, S.H. Current Status and Future Direction of Biodegradable Metallic and Polymeric Vascular Scaffolds for Next-Generation Stents. *Acta Biomater.* **2017**, *60*, 3–22. [CrossRef]
6. Hu, T.; Yang, C.; Lin, S.; Yu, Q.; Wang, G. Biodegradable Stents for Coronary Artery Disease Treatment: Recent Advances and Future Perspectives. *Mater. Sci. Eng. C* **2018**, *91*, 163–178. [CrossRef] [PubMed]
7. Zhao, J.; Mo, Z.; Guo, F.; Shi, D.; Han, Q.Q.; Liu, Q. Drug Loaded Nanoparticle Coating on Totally Bioresorbable PLLA Stents to Prevent In-stent Restenosis. *J. Biomed. Mater. Res.* **2018**, *106*, 88–95. [CrossRef] [PubMed]
8. Fan, W.; Johnson, D.M.; Feldman, M.D. Metallic Stents Coated with Bioabsorbable Polymers. *Card. Interv. Today* **2009**, *7*, 42–49.
9. Zong, J.; He, Q.; Liu, Y.; Qiu, M.; Wu, J.; Hu, B. Advances in the Development of Biodegradable Coronary Stents: A Translational Perspective. *Mater. Today Bio* **2022**, *16*, 100368. [CrossRef]
10. Wang, Q.; Fang, G.; Zhao, Y.; Wang, G.; Cai, T. Computational and Experimental Investigation into Mechanical Performances of Poly-L-Lactide Acid (PLLA) Coronary Stents. *J. Mech. Behav. Biomed. Mater.* **2017**, *65*, 415–427. [CrossRef]
11. Li, Y.; Shi, Y.; Lu, Y.; Li, X.; Zhou, J.; Zadpoor, A.A.; Wang, L. Additive Manufacturing of Vascular Stents. *Acta Biomater.* **2023**, *167*, 16–37. [CrossRef]
12. Hu, X.; Li, J.; Yang, J.; Cheng, J.; Zhang, Y.; Lang, J.; Liu, J.; Zhao, G.; Ni, Z. Focus on the Crucial Deformation Region to Adjust the Comprehensive Performance of Poly (L-Lactic Acid) Stent. *Int. J. Biol. Macromol.* **2023**, *230*, 123417. [CrossRef]
13. Zheng, J.-F.; Xi, Z.-W.; Li, Y.; Li, J.-N.; Qiu, H.; Hu, X.-Y.; Luo, T.; Wu, C.; Wang, X.; Song, L.-F.; et al. Long-Term Safety and Absorption Assessment of a Novel Bioresorbable Nitrided Iron Scaffold in Porcine Coronary Artery. *Bioact. Mater.* **2022**, *17*, 496–505. [CrossRef] [PubMed]
14. Zhang, H.; Zhang, W.; Qiu, H.; Zhang, G.; Li, X.; Qi, H.; Guo, J.; Qian, J.; Shi, X.; Gao, X.; et al. A Biodegradable Metal-Polymer Composite Stent Safe and Effective on Physiological and Serum-Containing Biomimetic Conditions. *Adv. Healthc. Mater.* **2022**, *11*, 2201740. [CrossRef]
15. Baek, S.-W.; Kim, D.-S.; Song, D.H.; Kim, H.B.; Lee, S.; Kim, J.H.; Lee, J.-K.; Hong, Y.J.; Park, C.G.; Han, D.K. Reduced Restenosis and Enhanced Re-Endothelialization of Functional Biodegradable Vascular Scaffolds by Everolimus and Magnesium Hydroxide. *Biomater. Res.* **2022**, *26*, 86. [CrossRef] [PubMed]
16. Qi, Y.; Li, X.; He, Y.; Zhang, D.; Ding, J. Mechanism of Acceleration of Iron Corrosion by a Polylactide Coating. *ACS Appl. Mater. Interfaces* **2019**, *11*, 202–218. [CrossRef] [PubMed]
17. Venkatraman, S.; Yingying, H.; Wong, Y.S. Bio-Absorbable Cardiovascular Implants: Status and Prognosis. *JOM* **2020**, *72*, 1833–1844. [CrossRef]
18. Lin, W.; Zhang, H.; Zhang, W.; Qi, H.; Zhang, G.; Qian, J.; Li, X.; Qin, L.; Li, H.; Wang, X.; et al. In Vivo Degradation and Endothelialization of an Iron Bioresorbable Scaffold. *Bioact. Mater.* **2021**, *6*, 1028–1039. [CrossRef]
19. Bakina, O.V.; Ivanova, L.Y.; Toropkov, N.E.; Senkina, E.I.; Lerner, M.I.; Glazkova, E.A.; Krinitsyn, M.G. Core–Shell Fe-Fe3O4 Nanoparticles for Synthesizing PLA Composites with Low Toxicity and High Radiopacity. *Phys. Mesomech.* **2022**, *25*, 270–278. [CrossRef]
20. Wei, H.; Menary, G.; Buchanan, F.; Yan, S.; Nixon, J. Experimental Characterisation on the Behaviour of PLLA for Stretch Blowing Moulding of Bioresorbable Vascular Scaffolds. *Int. J. Mater. Form.* **2021**, *14*, 375–389. [CrossRef]
21. Hu, X.; Cheng, J.; Zhao, G.; Hua, R.; Tian, Y.; Tao, J. Simulation and Experimental Investigation into Mechanical Behaviors of PLLA Stents during Deployment. In Proceedings of the 2020 Ural Symposium on Biomedical Engineering, Radioelectronics and Information Technology (USBEREIT), Yekaterinburg, Russia, 14–15 May 2020; IEEE: Yekaterinburg, Russia, 2020; pp. 203–206.
22. Chen, D.; Su, Z.; Weng, L.; Cao, L.; Chen, C.; Zeng, S.; Zhang, S.; Wu, T.; Hu, Q.; Xiao, J. Effect of Inflammation on Endothelial Cells Induced by Poly-L-Lactic Acid Degradation In Vitro and In Vivo. *J. Biomater. Sci. Polym. Ed.* **2018**, *29*, 1909–1919. [CrossRef]
23. Yang, F.; Niu, X.; Gu, X.; Xu, C.; Wang, W.; Fan, Y. Biodegradable Magnesium-Incorporated Poly(L-Lactic Acid) Microspheres for Manipulation of Drug Release and Alleviation of Inflammatory Response. *ACS Appl. Mater. Interfaces* **2019**, *11*, 23546–23557. [CrossRef]
24. Lee, H.I.; Heo, Y.; Baek, S.-W.; Kim, D.-S.; Song, D.H.; Han, D.K. Multifunctional Biodegradable Vascular PLLA Scaffold with Improved X-Ray Opacity, Anti-Inflammation, and Re-Endothelization. *Polymers* **2021**, *13*, 1979. [CrossRef] [PubMed]

25. Venezuela, J.; Dargusch, M.S. Addressing the Slow Corrosion Rate of Biodegradable Fe-Mn: Current Approaches and Future Trends. *Curr. Opin. Solid State Mater. Sci.* **2020**, *24*, 100822. [CrossRef]
26. Lin, W.; Qin, L.; Qi, H.; Zhang, D.; Zhang, G.; Gao, R.; Qiu, H.; Xia, Y.; Cao, P.; Wang, X.; et al. Long-Term In Vivo Corrosion Behavior, Biocompatibility and Bioresorption Mechanism of a Bioresorbable Nitrided Iron Scaffold. *Acta Biomater.* **2017**, *54*, 454–468. [CrossRef] [PubMed]
27. Fagali, N.S.; Grillo, C.A.; Puntarulo, S.; Fernández Lorenzo De Mele, M.A. Cytotoxicity of Corrosion Products of Degradable Fe-Based Stents: Relevance of pH and Insoluble Products. *Colloids Surf. B Biointerfaces* **2015**, *128*, 480–488. [CrossRef]
28. Wang, S.; Gu, R.; Wang, F.; Zhao, X.; Yang, F.; Xu, Y.; Yan, F.; Zhu, Y.; Xia, D.; Liu, Y. 3D-Printed PCL/Zn Scaffolds for Bone Regeneration with a Dose-Dependent Effect on Osteogenesis and Osteoclastogenesis. *Mater. Today Bio* **2022**, *13*, 100202. [CrossRef] [PubMed]
29. Cifuentes, S.C.; Gavilán, R.; Lieblich, M.; Benavente, R.; González-Carrasco, J.L. In Vitro Degradation of Biodegradable Polylactic Acid/Magnesium Composites: Relevance of Mg Particle Shape. *Acta Biomater.* **2016**, *32*, 348–357. [CrossRef]
30. Shuai, C.; Zan, J.; Qi, F.; Wang, G.; Liu, Z.; Yang, Y.; Peng, S. nMgO-Incorporated PLLA Bone Scaffolds: Enhanced Crystallinity and Neutralized Acidic Products. *Mater. Des.* **2019**, *174*, 107801. [CrossRef]
31. Cai, H.; Meng, J.; Li, X.; Xue, F.; Chu, C.; Guo, C.; Bai, J. In Vitro Degradation Behavior of Mg Wire/Poly(Lactic Acid) Composite Rods Prepared by Hot Pressing and Hot Drawing. *Acta Biomater.* **2019**, *98*, 125–141. [CrossRef]
32. Ko, K.-W.; Choi, B.; Kang, E.Y.; Shin, S.-W.; Baek, S.-W.; Han, D.K. The Antagonistic Effect of Magnesium Hydroxide Particles on Vascular Endothelial Activation Induced by Acidic PLGA Degradation Products. *Biomater. Sci.* **2021**, *9*, 892–907. [CrossRef] [PubMed]
33. Wang, T.; Lin, C.; Batalu, D.; Zhang, L.; Hu, J.; Lu, W. In Vitro Study of the PLLA-Mg65Zn30Ca5 Composites as Potential Biodegradable Materials for Bone Implants. *J. Magnes. Alloys* **2021**, *9*, 2009–2018. [CrossRef]
34. Jiang, D.; Ning, F.; Wang, Y. Additive Manufacturing of Biodegradable Iron-Based Particle Reinforced Polylactic Acid Composite Scaffolds for Tissue Engineering. *J. Mater. Process. Technol.* **2021**, *289*, 116952. [CrossRef]
35. Tettey, F.; Saudi, S.; Davies, D.; Shrestha, S.; Johnson, K.; Fialkova, S.; Subedi, K.; Bastakoti, B.P.; Sankar, J.; Desai, S.; et al. Fabrication and Characterization of Zn Particle Incorporated Fibrous Scaffolds for Potential Application in Tissue Healing and Regeneration. *ACS Appl. Mater. Interfaces* **2023**, *15*, 48913–48929. [CrossRef]
36. Qi, Y.; Qi, H.; He, Y.; Lin, W.; Li, P.; Qin, L.; Hu, Y.; Chen, L.; Liu, Q.; Sun, H.; et al. Strategy of Metal–Polymer Composite Stent to Accelerate Biodegradation of Iron-Based Biomaterials. *ACS Appl. Mater. Interfaces* **2018**, *10*, 182–192. [CrossRef]
37. Li, X.; Zhang, W.; Lin, W.; Qiu, H.; Qi, Y.; Ma, X.; Qi, H.; He, Y.; Zhang, H.; Qian, J.; et al. Long-Term Efficacy of Biodegradable Metal–Polymer Composite Stents After the First and the Second Implantations into Porcine Coronary Arteries. *ACS Appl. Mater. Interfaces* **2020**, *12*, 15703–15715. [CrossRef]
38. Zhang, W.; Gao, X.; Zhang, H.; Sun, G.; Zhang, G.; Li, X.; Qi, H.; Guo, J.; Qin, L.; Shi, D.; et al. Maglev-Fabricated Long and Biodegradable Stent for Interventional Treatment of Peripheral Vessels. *Nat. Commun.* **2024**, *15*, 7903. [CrossRef]
39. Gao, R.; Xu, B.; Sun, Z.; Guan, C.; Song, L.; Gao, L.; Li, C.; Cui, J.; Zhang, Y.; Dou, K.; et al. First-in-Human Evaluation of a Novel Ultrathin Sirolimus- Eluting Iron Bioresorbable Scaffold: 3-Year Outcomes of the IBS-FIM Trial. *EuroIntervention* **2023**, *19*, 222.
40. Huang, T.; Cheng, Y.; Zheng, Y. In Vitro Studies on Silver Implanted Pure Iron by Metal Vapor Vacuum Arc Technique. *Colloids Surf. B Biointerfaces* **2016**, *142*, 20–29. [CrossRef]
41. Ahadi, F.; Azadi, M.; Biglari, M.; Bodaghi, M.; Khaleghian, A. Evaluation of Coronary Stents: A Review of Types, Materials, Processing Techniques, Design, and Problems. *Heliyon* **2023**, *9*, e13575. [CrossRef]
42. Feng, P.; Yang, F.; Jia, J.; Zhang, J.; Tan, W.; Shuai, C. Mechanism and Manufacturing of 4D Printing: Derived and beyond the Combination of 3D Printing and Shape Memory Material. *Int. J. Extrem. Manuf.* **2024**, *6*, 062011. [CrossRef]
43. Feng, P.; Liu, L.; Yang, F.; Min, R.; Wu, P.; Shuai, C. Shape/Properties Collaborative Intelligent Manufacturing of Artificial Bone Scaffold: Structural Design and Additive Manufacturing Process. *Biofabrication* **2025**, *17*, 012005. [CrossRef] [PubMed]
44. Flege, C.; Vogt, F.; Höges, S.; Jauer, L.; Borinski, M.; Schulte, V.A.; Hoffmann, R.; Poprawe, R.; Meiners, W.; Jobmann, M.; et al. Development and Characterization of a Coronary Polylactic Acid Stent Prototype Generated by Selective Laser Melting. *J. Mater. Sci. Mater. Med.* **2013**, *24*, 241–255. [CrossRef] [PubMed]
45. Guerra, A.J.; Ciurana, J. 3D-Printed Bioabsorbable Polycaprolactone Stent: The Effect of Process Parameters on Its Physical Features. *Mater. Des.* **2018**, *137*, 430–437. [CrossRef]
46. Asyraf Azli, A.; Muhammad, N.; Mustafa Abdullah Albakri, M.; Fathullah Ghazali, M.; Zamree Abd Rahim, S.; Andrei Victor, S. Printing Parameter Optimization of Biodegradable PLA Stent Strut Thickness by Using Response Surface Methodology (RSM). *IOP Conf. Ser. Mater. Sci. Eng.* **2020**, *864*, 012154. [CrossRef]
47. Van Kampen, K.A.; Olaret, E.; Stancu, I.-C.; Moroni, L.; Mota, C. Controllable Four Axis Extrusion-Based Additive Manufacturing System for the Fabrication of Tubular Scaffolds with Tailorable Mechanical Properties. *Mater. Sci. Eng. C* **2021**, *119*, 111472. [CrossRef]

48. Guerra, A.; Cano, P.; Rabionet, M.; Puig, T.; Ciurana, J. 3D-Printed PCL/PLA Composite Stents: Towards a New Solution to Cardiovascular Problems. *Materials* **2018**, *11*, 1679. [CrossRef]
49. Yu, P.; Huang, S.; Yang, Z.; Liu, T.; Qilin, Z.; Feng, J.; Zeng, B. Biomechanical Properties of a Customizable TPU/PCL Blended Esophageal Stent Fabricated by 3D Printing. *Mater. Today Commun.* **2023**, *34*, 105196. [CrossRef]
50. Singh, J.; Singh, G.; Pandey, P.M. Multi-Objective Optimization of Solvent Cast 3D Printing Process Parameters for Fabrication of Biodegradable Composite Stents. *Int. J. Adv. Manuf. Technol.* **2021**, *115*, 3945–3964. [CrossRef]
51. Mahmud, Z.; Nasrin, A.; Hassan, M.; Gomes, V.G. 3D-PRINTED POLYMER Nanocomposites with Carbon Quantum Dots for Enhanced Properties and in Situ Monitoring of Cardiovascular Stents. *Polym. Adv. Technol.* **2022**, *33*, 980–990. [CrossRef]
52. Feng, P.; Shen, S.; Yang, L.; Kong, Y.; Yang, S.; Shuai, C. Vertical and Uniform Growth of MoS_2 Nanosheets on GO Nanosheets for Efficient Mechanical Reinforcement in Polymer Scaffold. *Virtual Phys. Prototyp.* **2023**, *18*, e2115384. [CrossRef]
53. Feng, P.; Tian, H.; Yang, F.; Peng, S.; Pan, H.; Shuai, C. Reduced Graphene Oxide-Mediated Electron-Hole Separation Using Titanium Dioxide Increases the Photocatalytic Antibacterial Activity of Bone Scaffolds. *Bio-Des. Manuf.* **2025**, *8*, 100–115. [CrossRef]
54. Jeong, Y.-J.; Jeong, S.; Kim, S.; Kim, H.J.; Jo, J.; Shanmugasundaram, A.; Kim, H.; Choi, E.; Lee, D.-W. 3D-Printed Cardiovascular Polymer Scaffold Reinforced by Functional Nanofiber Additives for Tunable Mechanical Strength and Controlled Drug Release. *Chem. Eng. J.* **2023**, *454*, 140118. [CrossRef]
55. Wang, C.; Yang, Y.; Ji, J.; Fang, Y.; Ouyang, L.; Zhang, L.; Sun, W. 3D-Printed Bioresorbable Stent Coated with Dipyridamole-Loaded Nanofiber for Restenosis Prevention and Endothelialization. *IJB* **2022**, *8*, 543. [CrossRef] [PubMed]
56. Ibrahim, Y.; Melenka, G.W.; Kempers, R. Additive Manufacturing of Continuous Wire Polymer Composites. *Manuf. Lett.* **2018**, *16*, 49–51. [CrossRef]
57. Güneş, M.; Çayiroğlu, İ. Mechanical Behaviour of 3D Printed Parts with Continuous Steel Wire Reinforcement. *El-Cezeri Fen. Ve Mühendislik Derg.* **2021**, *9*, 276–289. [CrossRef]
58. Li, L.; You, Q.; Liu, W.; Zeng, Q.; Zhou, C.; Wang, J.; Li, Z.; Li, K. Enhanced Flexural Performances of Cementitious Composite Beams with Continuously Graded Steel Fiber Distribution. *Mater. Des.* **2023**, *227*, 111728. [CrossRef]
59. Mishra, V.; Ror, C.K.; Negi, S.; Kar, S. Enhanced Fracture Toughness and Tensile Strength of 3D Printed Recycled ABS Composites Reinforced with Continuous Metallic Fiber for Load-Bearing Application. *RPJ* **2024**, *30*, 760–769. [CrossRef]
60. Mu, Q.; Dunn, C.K.; Wang, L.; Dunn, M.L.; Qi, H.J.; Wang, T. Thermal Cure Effects on Electromechanical Properties of Conductive Wires by Direct Ink Write for 4D Printing and Soft Machines. *Smart Mater. Struct.* **2017**, *26*, 045008. [CrossRef]
61. Ibrahim, Y.; Kempers, R. Effective Thermal Conductivity of 3D-Printed Continuous Wire Polymer Composites. *Prog. Addit. Manuf.* **2022**, *7*, 699–712. [CrossRef]
62. Shemelya, C.; Cedillos, F.; Aguilera, E.; Espalin, D.; Muse, D.; Wicker, R.; MacDonald, E. Encapsulated Copper Wire and Copper Mesh Capacitive Sensing for 3-D Printing Applications. *IEEE Sens. J.* **2015**, *15*, 1280–1286. [CrossRef]
63. Saleh, M.A.; Kempers, R.; Melenka, G.W. Fatigue Behavior and Electromechanical Properties of Additively Manufactured Continuous Wire Polymer Composites for Structural Health Monitoring. *Fatigue Fract. Eng. Mat. Struct.* **2022**, *45*, 2630–2645. [CrossRef]
64. Saleh, M.A.; Kempers, R.; Melenka, G.W. A Comparative Study on the Electromechanical Properties of 3D-Printed Rigid and Flexible Continuous Wire Polymer Composites for Structural Health Monitoring. *Sens. Actuators A Phys.* **2021**, *328*, 112764. [CrossRef]
65. Mohammed, M.I.; Wilson, D.; Gomez-Kervin, E.; Tang, B.; Wang, J. Investigation of Closed-Loop Manufacturing with Acrylonitrile Butadiene Styrene over Multiple Generations Using Additive Manufacturing. *ACS Sustain. Chem. Eng.* **2019**, *7*, 13955–13969. [CrossRef]
66. Kokubo, T.; Takadama, H. How Useful Is SBF in Predicting in Vivo Bone Bioactivity? *Biomaterials* **2006**, *27*, 2907–2915. [CrossRef]
67. Rojas-Martínez, L.E.; Flores-Hernandez, C.G.; López-Marín, L.M.; Martinez-Hernandez, A.L.; Thorat, S.B.; Reyes Vasquez, C.D.; Del Rio-Castillo, A.E.; Velasco-Santos, C. 3D Printing of PLA Composites Scaffolds Reinforced with Keratin and Chitosan: Effect of Geometry and Structure. *Eur. Polym. J.* **2020**, *141*, 110088. [CrossRef]
68. *ISO-13781-2017*; Implants for Surgery—Homopolymers, Copolymers and Blends on Poly(Lactide)—In Vitro Degradation Testing. ISO: Geneva, Switzerland, 2017.
69. Liu, J.; Wang, B.; Liu, W.; Hu, X.; Zhang, C.; Zhou, Z.; Lang, J.; Wu, G.; Zhang, Y.; Yang, J.; et al. Regulating Mechanical Performance of Poly (l-Lactide Acid) Stent by the Combined Effects of Heat and Aqueous Media. *Int. J. Biol. Macromol.* **2023**, *242*, 124987. [CrossRef]
70. Zhao, G.; Wang, B.; Li, X.; Liu, M.; Tian, Y.; Zhang, J.; Zhang, Y.; Cheng, J.; Yang, J.; Ni, Z. Evaluation of Poly (L-Lactic Acid) Monofilaments with High Mechanical Performance In Vitro Degradation. *J. Mater. Sci.* **2022**, *57*, 6361–6371. [CrossRef]
71. Weir, N.A.; Buchanan, F.J.; Orr, J.F.; Farrar, D.F.; Dickson, G.R. Degradation of Poly-L-Lactide. Part 2: Increased Temperature Accelerated Degradation. *Proc. Inst. Mech. Eng. Part H J. Eng. Med.* **2004**, *218*, 321–330. [CrossRef]

72. Srivastava, A.; Ahuja, R.; Bhati, P.; Singh, S.; Chauhan, P.; Vashisth, P.; Kumar, A.; Bhatnagar, N. Fabrication and Characterization of PLLA/Mg Composite Tube as the Potential Bioresorbable/Biodegradable Stent(BRS). *Materialia* **2020**, *10*, 100661. [CrossRef]
73. Srivastava, A.; Bhatnagar, N. Production and Characterisation of New Bioresorbable Radiopaque Mg–Zn–Y Alloy to Improve X-Ray Visibility of Polymeric Scaffolds. *J. Magnes. Alloys* **2022**, *10*, 1694–1703. [CrossRef]
74. Fiuza, C.; Polak-Kraśna, K.; Antonini, L.; Petrini, L.; Carroll, O.; Ronan, W.; Vaughan, T.J. An Experimental Investigation into the Physical, Thermal and Mechanical Degradation of a Polymeric Bioresorbable Scaffold. *J. Mech. Behav. Biomed. Mater.* **2022**, *125*, 104955. [CrossRef] [PubMed]
75. Hayman, D.; Bergerson, C.; Miller, S.; Moreno, M.; Moore, J.E. The Effect of Static and Dynamic Loading on Degradation of PLLA Stent Fibers. *J. Biomech. Eng.* **2014**, *136*, 081006. [CrossRef] [PubMed]
76. Naseem, R.; Zhao, L.; Eswaran, S.K.; Willcock, H. Characterization of Biodegradable Poly(L-lactide) Tube over Accelerated Degradation. *Polym. Eng. Sci.* **2020**, *60*, 1430–1436. [CrossRef]
77. Polak-Kraśna, K.; Abaei, A.R.; Shirazi, R.N.; Parle, E.; Carroll, O.; Ronan, W.; Vaughan, T.J. Physical and Mechanical Degradation Behaviour of Semi-Crystalline PLLA for Bioresorbable Stent Applications. *J. Mech. Behav. Biomed. Mater.* **2021**, *118*, 104409. [CrossRef]
78. *ASTM D3822/D3822M-14*; Standard Test Method for Tensile Properties of Single Textile Fibers. ASTM: West Conshohocken, PA, USA, 2020. [CrossRef]
79. Chen, Y.; Geever, L.M.; Killion, J.A.; Lyons, J.G.; Higginbotham, C.L.; Devine, D.M. Halloysite Nanotube Reinforced Polylactic Acid Composite. *Polym. Compos.* **2015**, *38*, 2166–2173. [CrossRef]
80. Liu, H.; Gong, K.; Portela, A.; Cao, Z.; Dunbar, R.; Chen, Y. Granule-Based Material Extrusion Is Comparable to Filament-Based Material Extrusion in Terms of Mechanical Performances of Printed PLA Parts: A Comprehensive Investigation. *Addit. Manuf.* **2023**, *75*, 103744. [CrossRef]
81. Kang, E.Y.; Lih, E.; Kim, I.H.; Joung, Y.K.; Han, D.K. Effects of Poly (L-Lactide-ε-Caprolactone) and Magnesium Hydroxide Additives on Physico-Mechanical Properties and Degradation of Poly (L-Lactic Acid). *Biomater. Res.* **2016**, *20*, 7. [CrossRef]
82. Jones, R.G. Dispersity in Polymer Science. *Polym. Int.* **2010**, *59*, 22. [CrossRef]
83. Liu, H.; Gong, K.; Portela, A.; Chyzna, V.; Yan, G.; Cao, Z.; Dunbar, R.; Chen, Y. Investigation of Distributed Recycling of Polylactic Acid over Multiple Generations via the Granule-Based Material Extrusion Process. *J. Clean. Prod.* **2024**, *436*, 140609. [CrossRef]
84. Chen, Y.; Liu, H.; Portela, A.; Higginbotham, C.; Devine, D. A Closed-Loop Process to Transform Mixed Plant Biomass Waste into Cellulose Acetate Bioplastic as Innovative Growing Substrates in Plant Cultivation. *Cellulose* **2024**, *31*, 9565–9581. [CrossRef]
85. Yan, G.; Cao, Z.; Devine, D.; Penning, M.; Gately, N.M. Physical Properties of Shellac Material Used for Hot Melt Extrusion with Potential Application in the Pharmaceutical Industry. *Polymers* **2021**, *13*, 3723. [CrossRef] [PubMed]
86. Cifuentes, S.C.; Frutos, E.; Benavente, R.; Lorenzo, V.; González-Carrasco, J.L. Assessment of Mechanical Behavior of PLA Composites Reinforced with Mg Micro-Particles through Depth-Sensing Indentations Analysis. *J. Mech. Behav. Biomed. Mater.* **2017**, *65*, 781–790. [CrossRef] [PubMed]
87. Yang, F.; Ye, X.; Zhong, J.; Lin, Z.; Wu, S.; Hu, Y.; Zheng, W.; Zhou, W.; Wei, Y.; Dong, X. Recycling of Waste Crab Shells into Reinforced Poly (Lactic Acid) Biocomposites for 3D Printing. *Int. J. Biol. Macromol.* **2023**, *234*, 122974. [CrossRef] [PubMed]
88. Chen, Y.; Murphy, A.; Scholz, D.; Geever, L.M.; Lyons, J.G.; Devine, D.M. Surface-Modified Halloysite Nanotubes Reinforced Poly(Lactic Acid) for Use in Biodegradable Coronary Stents. *J. Appl. Polym. Sci.* **2018**, *135*, 46521. [CrossRef]
89. Zhou, Z.; Salaoru, I.; Morris, P.; Gibbons, G.J. Additive Manufacturing of Heat-Sensitive Polymer Melt Using a Pellet-Fed Material Extrusion. *Addit. Manuf.* **2018**, *24*, 552–559. [CrossRef]
90. Zhang, Y.; Roux, C.; Rouchaud, A.; Meddahi-Pellé, A.; Gueguen, V.; Mangeney, C.; Sun, F.; Pavon-Djavid, G.; Luo, Y. Recent Advances in Fe-Based Bioresorbable Stents: Materials Design and Biosafety. *Bioact. Mater.* **2024**, *31*, 333–354. [CrossRef]
91. Shi, X.; Zhang, L.; Liu, Y.; Wang, J.; Zhang, G.; Qi, H.; Zhang, W.; Zhang, D.; Wang, J. Study on the Chronic Toxicity and Carcinogenicity of Iron-Based Bioabsorbable Stents. *Nanotechnol. Rev.* **2023**, *12*, 20220507. [CrossRef]
92. Wu, J.; Lu, X.; Tan, L.; Zhang, B.; Yang, K. Effect of Hydrion Evolution by Polylactic-*Co*-Glycolic Acid Coating on Degradation Rate of Pure Iron: Effect of Hydrion Evolution. *J. Biomed. Mater. Res.* **2013**, *101*, 1222–1232. [CrossRef]
93. Shi, D.; Kang, Y.; Zhang, G.; Gao, C.; Lu, W.; Yang, C.; Zou, H.; Jiang, H. A Comparative Study on In Vitro Degradation Behavior of PLLA-Based Copolymer Monofilaments. *Polym. Degrad. Stab.* **2018**, *158*, 148–156. [CrossRef]
94. Tian, Y.; Zhang, J.; Cheng, J.; Wu, G.; Zhang, Y.; Ni, Z.; Zhao, G. A Poly(L-lactic Acid) Monofilament with High Mechanical Properties for Application in Biodegradable Biliary Stents. *J. Appl. Polym. Sci.* **2021**, *138*, 49656. [CrossRef]
95. Khalaj Amnieh, S.; Mosaddegh, P.; Mashayekhi, M.; Kharaziha, M. Biodegradation Evaluation of Poly (Lactic Acid) for Stent Application: Role of Mechanical Tension and Temperature. *J. Appl. Polym. Sci.* **2021**, *138*, 50389. [CrossRef]
96. Zamiri, P.; Kuang, Y.; Sharma, U.; Ng, T.F.; Busold, R.H.; Rago, A.P.; Core, L.A.; Palasis, M. The Biocompatibility of Rapidly Degrading Polymeric Stents in Porcine Carotid Arteries. *Biomaterials* **2010**, *31*, 7847–7855. [CrossRef] [PubMed]
97. Abaei, A.R.; Vaughan, T.J.; Ronan, W. Micromechanical Modelling of Biodegradable Semi-Crystalline Polymers: The Evolution of Anisotropic Mechanical Properties during Degradation. *Int. J. Solids Struct.* **2023**, *279*, 112366. [CrossRef]

98. Wang, A.; Venezuela, J.; Dargusch, M.S. Enhancing the Corrodibility of Biodegradable Iron and Zinc Using Poly(Lactic) Acid (PLA) Coating for Temporary Medical Implant Applications. *Prog. Org. Coat.* **2023**, *174*, 107301. [CrossRef]
99. Chausse, V.; Iglesias, C.; Bou-Petit, E.; Ginebra, M.-P.; Pegueroles, M. Chemical vs Thermal Accelerated Hydrolytic Degradation of 3D-Printed PLLA/PLCL Bioresorbable Stents: Characterization and Influence of Sterilization. *Polym. Test.* **2023**, *117*, 107817. [CrossRef]
100. Shuai, C.; Wang, Z.; Zhang, H.; Jia, J.; Huang, L.; Wang, D.; Chen, S.; Feng, P. Biosoluble Ceramic Fiber Reinforced Poly(L-Lactic Acid) Bone Scaffold: Degradation and Bioactivity. *npj Mater. Degrad.* **2022**, *6*, 87. [CrossRef]
101. Oosterbeek, R.N.; Kwon, K.-A.; Duffy, P.; McMahon, S.; Zhang, X.C.; Best, S.M.; Cameron, R.E. Tuning Structural Relaxations, Mechanical Properties, and Degradation Timescale of PLLA during Hydrolytic Degradation by Blending with PLCL-PEG. *Polym. Degrad. Stab.* **2019**, *170*, 109015. [CrossRef]
102. Lin, W.; Zhang, G.; Cao, P.; Zhang, D.; Zheng, Y.; Wu, R.; Qin, L.; Wang, G.; Wen, T. Cytotoxicity and Its Test Methodology for a Bioabsorbable Nitrided Iron Stent: Cytocompatibility of Bioabsorbable Iron-Based Materials. *J. Biomed. Mater. Res.* **2015**, *103*, 764–776. [CrossRef]
103. Ekinci, A.; Gleadall, A.; Johnson, A.A.; Li, L.; Han, X. Mechanical and Hydrolytic Properties of Thin Polylactic Acid Films by Fused Filament Fabrication. *J. Mech. Behav. Biomed. Mater.* **2021**, *114*, 104217. [CrossRef]
104. Moetazedian, A.; Gleadall, A.; Han, X.; Ekinci, A.; Mele, E.; Silberschmidt, V.V. Mechanical Performance of 3D Printed Polylactide during Degradation. *Addit. Manuf.* **2021**, *38*, 101764. [CrossRef]
105. Zhao, G.; Li, X.; Tian, Y.; Wu, G.; Zhang, Y.; Jiang, W.; Yang, J.; Ni, Z. Poly(l-Lactic Acid) Monofilaments for Biodegradable Braided Self-Expanding Stent. *J. Mater. Sci.* **2021**, *56*, 12383–12393. [CrossRef]
106. Van de Voorde, B.; Katalagarianakis, A.; Huysman, S.; Toncheva, A.; Raquez, J.M.; Duretek, I.; Holzer, C.; Cardon, L.; Bernaerts, K.V.; Van Hemelrijck, D.; et al. Effect of Extrusion and Fused Filament Fabrication Processing Parameters of Recycled Poly(Ethylene Terephthalate) on the Crystallinity and Mechanical Properties. *Addit. Manuf.* **2022**, *50*, 102518. [CrossRef]
107. Ibrahim, Y.; Melenka, G.W.; Kempers, R. Fabrication and Tensile Testing of 3D Printed Continuous Wire Polymer Composites. *RPJ* **2018**, *24*, 1131–1141. [CrossRef]
108. Li, X.; Hu, J.; Yu, Z.; Liu, M.; Xiao, X.; Qin, G.; Yang, L.; Zhang, E. A Study on the In Vitro and In Vivo Degradation Behaviour and Biocompatibility of a Mg-Mn-Zn Alloy with PLLA and Micro Arc Oxidation Composite Coating. *Surf. Coat. Technol.* **2023**, *471*, 129894. [CrossRef]
109. Shen, Y.; Tang, C.; Sun, B.; Zhang, Y.; Sun, X.; EL-Newehy, M.; EL-Hamshary, H.; Morsi, Y.; Gu, H.; Wang, W.; et al. 3D Printed Personalized, Heparinized and Biodegradable Coronary Artery Stents for Rabbit Abdominal Aorta Implantation. *Chem. Eng. J.* **2022**, *450*, 138202. [CrossRef]
110. Wang, B.; Liu, M.; Liu, J.; Tian, Y.; Liu, W.; Wu, G.; Cheng, J.; Zhang, Y.; Zhao, G.; Ni, Z. Key Factors of Mechanical Strength and Toughness in Oriented Poly(L-Lactic Acid) Monofilaments for a Bioresorbable Self-Expanding Stent. *Langmuir* **2022**, *38*, 13477–13487. [CrossRef] [PubMed]
111. Oliver, A.A.; Sikora-Jasinska, M.; Demir, A.G.; Guillory, R.J. Recent Advances and Directions in the Development of Bioresorbable Metallic Cardiovascular Stents: Insights from Recent Human and In Vivo Studies. *Acta Biomater.* **2021**, *127*, 1–23. [CrossRef]
112. Lan, Z.; Lyu, Y.; Xiao, J.; Zheng, X.; He, S.; Feng, G.; Zhang, Y.; Wang, S.; Kislauskis, E.; Chen, J.; et al. Novel Biodegradable Drug-Eluting Stent Composed of Poly-L-Lactic Acid and Amorphous Calcium Phosphate Nanoparticles Demonstrates Improved Structural and Functional Performance for Coronary Artery Disease. *J. Biomed. Nanotechnol.* **2014**, *10*, 1194–1204. [CrossRef]
113. Duek, E.A.R.; Zavaglia, C.A.C.; Belangero, W.D. In Vitro Study of Poly(Lactic Acid) Pin Degradation. *Polymer* **1999**, *40*, 6465–6473. [CrossRef]
114. Tsuji, H. In Vitro Hydrolysis of Blends from Enantiomeric Poly(Lactide)s Part 1. Well-Stereo-Complexed Blend and Non-Blended Films. *Polymer* **2000**, *41*, 3621–3630. [CrossRef]
115. Tsuji, H. In Vitro Hydrolysis of Blends from Enantiomeric Poly(Lactide)s. Part 4: Well-Homo-Crystallized Blend and Nonblended Films. *Biomaterials* **2003**, *24*, 537–547. [CrossRef] [PubMed]
116. Saha, S.K.; Tsuji, H. Effects of Molecular Weight and Small Amounts of D-Lactide Units on Hydrolytic Degradation of Poly(l-Lactic Acid)s. *Polym. Degrad. Stab.* **2006**, *91*, 1665–1673. [CrossRef]
117. Bowen, P.K.; Drelich, J.; Goldman, J. Zinc Exhibits Ideal Physiological Corrosion Behavior for Bioabsorbable Stents. *Adv. Mater.* **2013**, *25*, 2577–2582. [CrossRef] [PubMed]
118. Mostaed, E.; Sikora-Jasinska, M.; Drelich, J.W.; Vedani, M. Zinc-Based Alloys for Degradable Vascular Stent Applications. *Acta Biomater.* **2018**, *71*, 1–23. [CrossRef]
119. Bowen, P.K.; Shearier, E.R.; Zhao, S.; Guillory, R.J.; Zhao, F.; Goldman, J.; Drelich, J.W. Biodegradable Metals for Cardiovascular Stents: From Clinical Concerns to Recent Zn-alloys. *Adv. Healthc. Mater.* **2016**, *5*, 1121–1140. [CrossRef]
120. Shen, Y.; Tang, C.; Sun, B.; Wu, Y.; Yu, X.; Cui, J.; Zhang, M.; EL-Newehy, M.; EL-Hamshary, H.; Barlis, P.; et al. Development of 3D Printed Biodegradable, Entirely X-ray Visible Stents for Rabbit Carotid Artery Implantation. *Adv. Healthc. Mater.* **2024**, *13*, 2304293. [CrossRef]

121. Peuster, M.; Hesse, C.; Schloo, T.; Fink, C.; Beerbaum, P.; Von Schnakenburg, C. Long-Term Biocompatibility of a Corrodible Peripheral Iron Stent in the Porcine Descending Aorta. *Biomaterials* **2006**, *27*, 4955–4962. [CrossRef]
122. Wang, H.-T.; Chiang, P.-C.; Tzeng, J.-J.; Wu, T.-L.; Pan, Y.-H.; Chang, W.-J.; Huang, H.-M. In Vitro Biocompatibility, Radiopacity, and Physical Property Tests of Nano-Fe3O4 Incorporated Poly-l-Lactide Bone Screws. *Polymers* **2017**, *9*, 191. [CrossRef]
123. Li, M.; Deng, D.; Chen, Z.; Liu, W.; Zhao, G.; Zhang, Y.; Yang, F.; Ni, Z. Magnetic Nanoparticle Loaded Biodegradable Vascular Stents for Magnetic Resonance Imaging and Long-Term Visualization. *J. Mater. Chem. B* **2023**, *11*, 3669–3678. [CrossRef]

Disclaimer/Publisher's Note: The statements, opinions and data contained in all publications are solely those of the individual author(s) and contributor(s) and not of MDPI and/or the editor(s). MDPI and/or the editor(s) disclaim responsibility for any injury to people or property resulting from any ideas, methods, instructions or products referred to in the content.